Cell Chemical Biology
Article

Multi-metal Restriction by Calprotectin Impacts *De Novo* Flavin Biosynthesis in *Acinetobacter baumannii*

Jiefei Wang,[1,2,9] Zachery R. Lonergan,[3,9] Giovanni Gonzalez-Gutierrez,[2] Brittany L. Nairn,[3] Christina N. Maxwell,[4,5,6] Yixiang Zhang,[1,7] Claudia Andreini,[8] Jonathan A. Karty,[1] Walter J. Chazin,[4,5,6] Jonathan C. Trinidad,[1,7,*] Eric P. Skaar,[3,*] and David P. Giedroc[1,2,10,*]

[1]Department of Chemistry, Indiana University, Bloomington, IN 47405, USA
[2]Department of Molecular and Cellular Biochemistry, Indiana University, Bloomington, IN 47405, USA
[3]Department of Pathology, Microbiology, and Immunology, Vanderbilt University Medical Center, Nashville, TN 37232, USA
[4]Center for Structural Biology, Vanderbilt University, Nashville, TN 37232, USA
[5]Department of Biochemistry, Vanderbilt University, Nashville, TN 37205, USA
[6]Department of Chemistry, Vanderbilt University, Nashville, TN 37235, USA
[7]Laboratory for Biological Mass Spectrometry, Department of Chemistry, Indiana University, Bloomington, IN 47405, USA
[8]Magnetic Resonance Centre (CERM), University of Florence, Florence, 50019 Sesto Fiorentino, Italy
[9]These authors contributed equally
[10]Lead Contact
*Correspondence: trinidad@indiana.edu (J.C.T.), eric.skaar@vumc.org (E.P.S.), giedroc@indiana.edu (D.P.G.)
https://doi.org/10.1016/j.chembiol.2019.02.011

SUMMARY

Calprotectin (CP) inhibits bacterial viability through extracellular chelation of transition metals. However, how CP influences general metabolism remains largely unexplored. We show here that CP restricts bioavailable Zn and Fe to the pathogen *Acinetobacter baumannii*, inducing an extensive multi-metal perturbation of cellular physiology. Proteomics reveals severe metal starvation, and a strain lacking the candidate Zn^{II} metallochaperone ZigA possesses altered cellular abundance of multiple essential Zn-dependent enzymes and enzymes in *de novo* flavin biosynthesis. The Δ*zigA* strain exhibits decreased cellular flavin levels during metal starvation. Flavin mononucleotide provides regulation of this biosynthesis pathway, via a 3,4-dihydroxy-2-butanone 4-phosphate synthase (RibB) fusion protein, RibBX, and authentic RibB. We propose that RibBX ensures flavin sufficiency under CP-induced Fe limitation, allowing flavodoxins to substitute for Fe-ferredoxins as cell reductants. These studies elucidate adaptation to nutritional immunity and define an intersection between metallostasis and cellular metabolism in *A. baumannii*.

INTRODUCTION

Transition metals are important to microbial physiology and execute key catalytic, structural, and regulatory functions that broadly influence all phases of cellular physiology. The mammalian host takes advantage of this essentiality by restricting growth of invading bacteria through a process termed nutritional immunity, in which transition metals are withheld from microbial invaders by mammalian metal-binding proteins (Damo et al., 2013; Hood and Skaar, 2012; Weinberg, 1975). Host neutrophils and other immune cells secrete a number of metal-chelating innate immune proteins at sites of infection, including S100-family proteins. One such protein is calprotectin (CP; S100A8/A9 oligomer), which is a versatile extracellular metal-sequestering protein that forms highly thermodynamically and/or kinetically stable coordination complexes with Zn^{II}, Mn^{II}, Fe^{II}, and Ni^{II} (Damo et al., 2013; Nakashige et al., 2015; Nakashige et al., 2017). CP-dependent metal binding restricts the availability of these metals and inhibits the growth of pathogens (Corbin et al., 2008; Zygiel and Nolan, 2018). While the physiological impact of CP is expected to be niche and pathogen dependent, little is known about how CP-induced stress affects metabolism in different pathogens (Besold et al., 2017; Wakeman et al., 2016).

Acinetobacter baumannii is a Gram-negative bacterial pathogen commonly associated with hospital-acquired infections and is a leading cause of ventilator-associated pneumonia (Doyle et al., 2011). Increasing reports of community-acquired and multi-drug-resistant *Acinetobacter* infections have attracted considerable public attention (Harding et al., 2018). CP inhibits *A. baumannii* growth and protects against *A. baumannii* infection in a mouse model of pneumonia (Hood et al., 2012). A transposon mutagenesis screen identified a strain lacking the Zn uptake transporter *znuB*, which is regulated by the Zn uptake repressor Zur, as being defective for growth in the presence of CP and is consistent with the finding that CP induces Zn but not Mn starvation (Hood et al., 2012). Subsequent transcriptomic experiments with the Δ*zur* strain identified the Zur regulon as well as other Zn-responsive genes, which included the putative Zn^{II} chaperone, ZigA (Zur-induced GTPase A) (Mortensen et al., 2014); follow-up work revealed that the Δ*zigA* strain is sensitive to CP stress (Mortensen et al., 2014; Nairn et al., 2016). While the importance of Zur and the induction of known Zur-regulated

genes in response to CP has been defined (Mortensen et al., 2014; Nairn et al., 2016), it is not yet known how other metal homeostasis and metabolism systems are perturbed by CP stress.

Elucidating a global understanding of CP-induced perturbations in bacterial transition metal distribution networks and downstream physiological changes in cellular metabolism is important but remains largely understudied (Zygiel and Nolan, 2018). Cells must alter their metabolism when they are metal starved. A number of essential metabolic pathways are *initiated* with a Zn^{II} metalloenzyme, including the biosynthesis of folate, queuosine-tRNA, riboflavin, and, in some organisms, tetrahydrobiopterin (Phillips et al., 2012). Given that enzymes that require Zn^{II} or another transition metal for activity are positioned at critical hubs in cellular physiology, it is unclear how bacterial cells balance cellular metabolism under CP-induced metal-deficient conditions. In addition, while studies of how cells regulate metal transport are widespread, these studies have tended to underestimate how intermediary metabolism adapts to host-induced metal starvation. In *A. baumannii*, CP moderately induces the genes required for *L*-histidine catabolism (*hut*), which are proposed to contribute to the release of Zn^{II} from Zn-His_2 complexes, thus increasing access by Zn^{II}-dependent processes under extreme Zn limitation (Nairn et al., 2016). In addition, iron starvation has been linked to induction of flavin biosynthesis in bacteria and eukaryotes where substitution of flavodoxins for ferredoxins as cellular reductants was proposed (LaRoche et al., 1996; Tognetti et al., 2007). A global, systems-level view of how CP affects metabolic processes is clearly needed.

The studies presented here describe the metabolic impact of nutritional immunity in *A. baumannii*. Using *A. baumannii* Δ*zigA* as a tool to exacerbate multi-metal (Zn and Fe) starvation induced by CP, we observe an incrementally increased abundance of two related enzymes of the flavin biosynthesis pathway, RibBX and RibB, consistent with cellular efforts to ensure sufficient flavin supply under conditions of extreme metal limitation or misallocation, predicted on the basis of global changes in the Zn^{II} proteome. These observations are consistent with our discovery that Δ*zigA* is unable to maintain appropriate flavin abundance during metal starvation and that *ribBX* contributes to the ability of *A. baumannii* to synthesize flavins and overcome nutrient metal limitation. Our findings support a dual regulatory model explaining how *A. baumannii* maintains cellular flavin sufficiency required for central metabolic processes in an effort to overcome CP-induced metal starvation. Our studies also validate ongoing efforts to develop pharmacological strategies against *A. baumannii* by identifying flavin biosynthetic enzymes as required to survive nutrient limitation. Notably, these enzymes are established antimicrobial targets in other bacterial pathogens, emphasizing the general significance of these findings (Islam et al., 2015).

RESULTS

Calprotectin Induces Multi-metal Restriction in *A. baumannii*

Although CP is known to induce Zn^{II} starvation in *A. baumannii* (Hood et al., 2012), the extent to which other metal homeostasis systems are influenced by CP is not known. To address the question, a global transcriptomic analysis (RNA sequencing; RNA-seq) (Figure 1) and a proteomic analysis (Figure 2) were performed on a wild-type (WT) strain grown in the presence or absence of physiologically relevant concentrations of CP (Clohessy and Golden, 1995). We first measured the metal concentration in the culture medium (60% LB + CP buffer) with or without 200 μg/mL CP (Figures 1A and S1). CP notably depletes the culture medium of the major metals Zn and Fe, with no effect on Cu. Mn and Co are also significantly decreased by CP.

We next performed a transcriptomic analysis (Figure 1B; Table S1) and a liquid chromatography-tandem mass spectrometry (LC-MS/MS), label-free proteomic analysis, in which we detected up to 1,094 proteins in these cytoplasmic lysates, which corresponds to 28.9% of the *A. baumannii* proteome (Figures 2 and S2A–S2D; Table S2). Of the 67 genes that are significantly increased in CP-treated relative to untreated WT cells, 14 also displayed increased transcription in a strain lacking the Zn^{II}-responsive transcriptional regulator *zur* (Δ*zur*) (Mortensen et al., 2014) (Figure 1B). Furthermore, among the most upregulated genes are Zur-regulated targets, including genes involved in cellular Zn uptake and *zigA* (Mortensen et al., 2014); increased abundance of ZigA is further confirmed in the proteomic analysis (Figure 2D).

Both experiments reveal that CP induces both Zn^{II} and Fe starvation. Relative to Fe starvation, the RNA-seq (Figure 1B) reveals a dramatically decreased transcription of genes encoding bacterioferritins, but increased transcription of genes involved in the global Fe-limitation response, including *feoAB*, which brings Fe^{II} into the cell, and Fe^{III}-siderophore receptors, as confirmed by qRT-PCR (Figure 1C). Consistently, putative achromobactin and acinetobactin siderophore biosynthesis/utilization proteins become more cell abundant with CP stress, some at a level approaching that of ZigA (Figure 2D). The upregulation of siderophore uptake systems was further confirmed by robust siderophore production following CP exposure (Figures S2E–S2F). In addition, changes were observed in cellular abundances of Fe proteins, including those involved in Fe-S cluster biogenesis (IscS and IscR), and the fumarase (FumA) (Figures 2C and 2D) characterized as part of the Fe-sparing response (Lee and Helmann, 2007). These results are consistent with a significant CP-mediated impact on Fe homeostasis and suggest a strong perturbation of Fe metabolism in *A. baumannii.*

These findings also revealed an unexpected intersection of CP-induced Zn and Fe starvation with Cu homeostasis. We observed a transcriptomic downregulation of a putative Cu importer *oprC* (outer membrane porin, A1S_0170) (Yoneyama and Nakae, 1996) (Figure 1) coupled with detection of a previously unannotated protein, V5VEM0, a putative copper storage protein (Csp) (Straw et al., 2018), only in CP-treated cells (Figure 2D; Table S3). These findings suggest that Zn- and Fe-starved *A. baumannii* may decrease bioavailability of Cu under these CP-treatment conditions.

Cell-Abundant Metalloproteins Induced by CP Stress Are Established Therapeutic Targets

We also found 26 proteins significantly increased in normalized cellular abundance in CP-treated lysates, including two known Zn^{II} metalloenzymes (Figure 2C), β-carbonic anhydrase (MtcA2), which may be important for survival, invasion, and pathogenicity (Aspatwar et al., 2018), and succinyl-diaminopimelate

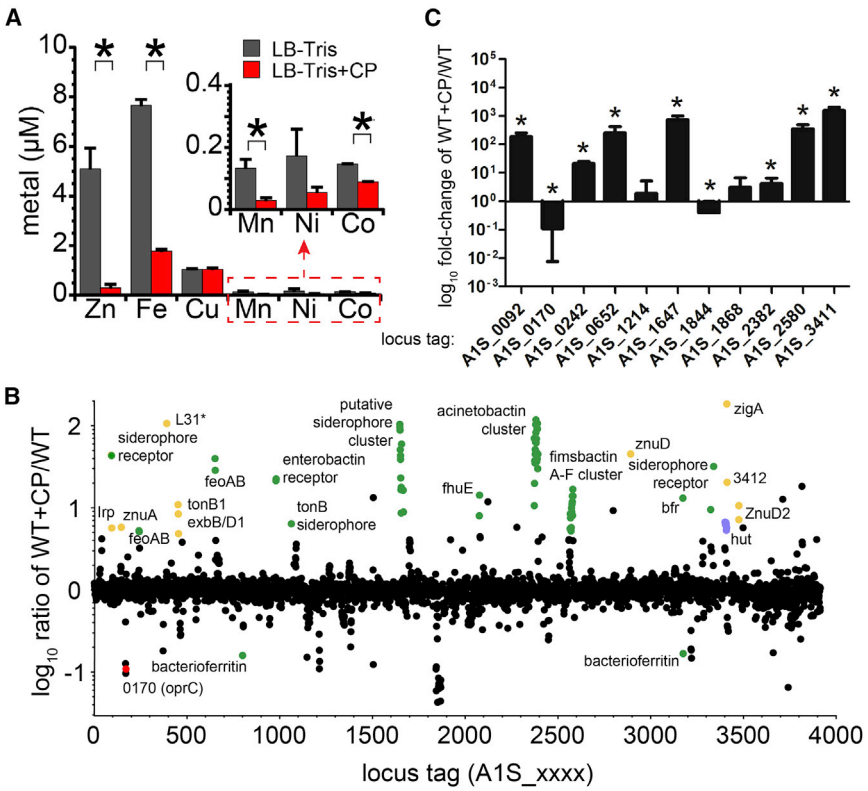

Figure 1. Transcriptomic Analysis of WT and WT + CP *A. baumannii*

(A) Metal content in the LB-Tris buffer growth medium treated with 0 (gray) or 200 μg/mL CP (red).

(B) RNA-seq analysis of untreated WT versus 200 μg/mL calprotectin-treated WT (WT + CP) *A. baumannii* cells from four biological replicates. The fold change in expression for each locus tag is indicated (see Table S1 for a complete list of genes). Gene names are indicated according to the NCBI annotation; otherwise, the locus tag (A1S_xxxx where "xxxx" represents the locus tag number) is indicated. Genes regulated by the Zn uptake regulator (Zur) (yellow symbols), involved in Fe homeostasis (green symbols), involved in Cu uptake (red symbols), and associated with the histidine utilization (*hut*) operon (purple circles) (Nairn et al., 2016) are highlighted.

(C) qRT-PCR validation of selected genes identified by RNA-seq. A1S_0092, putative ferric siderophore uptake protein; A1S_0170, OprC outer membrane copper receptor; A1S_0242, FeoA; A1S_0652, FeoA; A1S_1214, benzoate 1,2-dioxygenase β subunit; A1S_1647, siderophore biosynthesis protein; A1S_1844, CatC3, muconolactone δ-isomerase; A1S_1868, porin for benzoate transport; A1S_2382, BasD; A1S_2580, siderophore biosynthesis protein.

*$p < 0.05$ as determined by Student's t test with hypothetical value of 1. Data are the means combined from three independent experiments ±SD. See also Figure S1; Table S1.

desuccinylase (DapE), which is involved in the synthesis of *meso*-diaminopimelate, a component of the peptidoglycan of all Gram-negative bacteria. Fifteen proteins were detected only in CP-treated cells at high cellular levels (Figure 2D), including the Zn metalloenzyme QueD, which is involved in queuosine-tRNA biosynthesis (Vinayak and Pathak, 2010), and ZigA, which is required for bacterial growth under Zn-limiting conditions and disseminated infections in mice (Nairn et al., 2016).

A. baumannii ΔzigA Is More Susceptible to CP-Induced Metal Starvation

As the candidate metallochaperone ZigA (Nairn et al., 2016) is among the most abundant metalloproteins that are detected *only* in CP-treated WT cells (*vide infra*), investigation of how the Δ*zigA* strain adapts to CP stress relative to the WT strain may identify crippled ZigA-dependent processes. The addition of CP gave rise to a significant decrease in growth yield of exponentially growing cells ($t = 4$ h), but only in the Δ*zigA* strain (Figures 3A, S3A, and S3B). CP induces a measurable decrease in total cell-associated Zn and Fe, but only in the WT strain (Figure 3B), a finding consistent with transcriptomic and proteomic analysis (Figures 1 and 2). In addition, the Δ*zigA* strain exhibits increased expression of the Zn uptake genes (Nairn et al., 2016), which may account for these findings. Total cell-associated Cu is also lower only in the WT strain (Figure 3C), consistent with the downregulation of *oprC* (Figure 1C). The Δ*zigA* strain, in contrast, takes up slightly more Mn and Ni when treated with CP (Figure 3C). These CP-induced trends in growth yield and in cellular metal content largely persist at 6 and 8 h of growth (Figures S3C–S3F). These results reveal that CP restricts Zn and Fe availability and the loss of ZigA has little further impact on total cell-associated metal, but with a perturbation in metal allocation to cellular targets. This is representative of "adaptive" physiology, since metallation can increase the stability of metalloproteins (Figure 3D).

As an effort to monitor a perturbation in metal allocation, we found that the proteomic profiles of unstressed WT and Δ*zigA* cells are extremely similar but show marked differences in the presence of CP (Figures 4A–4C, S4A, and S4B; Table S4). To understand these differences, a bioinformatics approach was employed to predict the entire Zn proteome of *A. baumannii* (Table S5). We predicted 213 Zn proteins, corresponding to ≈5% of the proteome, similar to predictions for *E. coli* (Andreini et al., 2006), and these proteins are anticipated to have an impact on a considerable range of cellular metabolism (Figure S4C), with 84 high-probability Zn proteins were detected in at least three replicates in the proteomic analysis (Figure S4D). Overall, zinc proteins are modestly more abundant (by protein count) in the WT relative to the Δ*zigA* strain in the presence of CP, including MtcA2 (Figure 4B) and the global Fe uptake regulator (Fur) (Figure S3E), with the striking exception of tRNA-guanosine transglycosylase (Tgt), involved in queuosine-tRNA biosynthesis (Vinayak and Pathak, 2010), which is detected only in CP-treated Δ*zigA* cells at high abundance (Figure 4C; Table S4).

A Dual Regulatory Model of Flavin Biosynthesis in *A. baumannii* in Response to CP

We found that RibB is detected only in CP-stressed Δ*zigA* and is undetectable in the WT strain under both conditions (Figures 4C

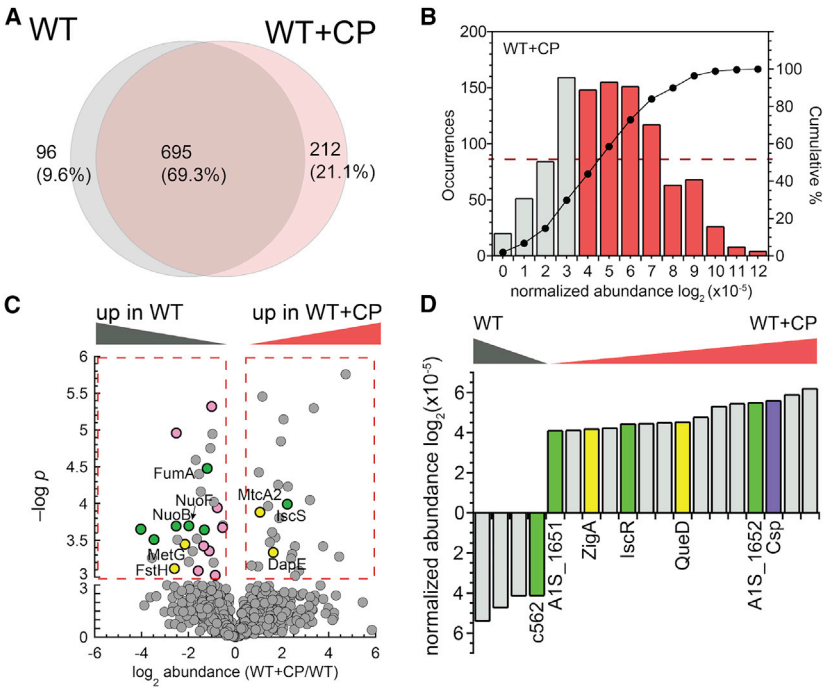

Figure 2. LC-MS/MS Proteomic Analysis for WT and WT + CP *A. baumannii*

Protein profiles of untreated WT versus 200 μg/mL calprotectin-treated WT (WT + CP) *A. baumannii* cells from four biological replicates.

(A) Venn diagram for proteins detected at least three times in four replicates.

(B) Histogram plot of the distribution of normalized abundance for all proteins detected in the untreated WT strain, as representative of all four growth conditions (see Figures S2A and S2D). The top-most 50% abundant proteins are indicated with a red dashed line with the bars shaded red.

(C) Volcano plot for proteins detected at least three times for each condition among four biological replicates. The significance threshold was set at $p \leq 0.001$ and fold change in protein abundance at >1.3 as shown in the red dashed-line box for proteins that are up (right top) and down (left top) in WT + CP. Filled circles are shaded yellow for Zn-binding proteins, green for proteins involved in iron homeostasis, purple for Cu-binding proteins, and pink for proteins involved in transcription or translation for Figure (C) and (D).

(D) Proteins that are strongly changed under WT + CP conditions. Normalized abundance for proteins that was detected only in WT or WT + CP in all four replicates with the significance threshold set at the top-most 50% abundance is shown (see Figure 2B).

See also Figure S2; Tables S2 and S3.

and 4D). Like many bacteria, *A. baumannii* synthesizes riboflavin, flavin mononucleotide (FMN), and flavin adenine dinucleotide (FAD) from guanosine 5′-triphosphate (GTP) via the actions of the Zn^{II}-dependent GTP cyclohydrolase II (GCHII), encoded by *ribA*, and from ribulose-5′-phosphate (Ru5P), a product of the pentose phosphate pathway, via the activity of 3,4-dihydroxy-2-butanone 4-phosphate synthase (DHBPS), encoded by *ribB* (Figure 4E). In addition to an impact of CP on Zn-protein abundance (*vide infra*), while RibA abundance is unchanged by CP treatment, an uncharacterized RibB-domain-containing fusion protein that we designate RibBX is more abundant in the WT strain in the presence of CP ($p \leq 0.05$) (Figures 4D and S4F), indicating that the two RibB enzymes associated with riboflavin biosynthesis (*rib*) also play a role in the response to CP.

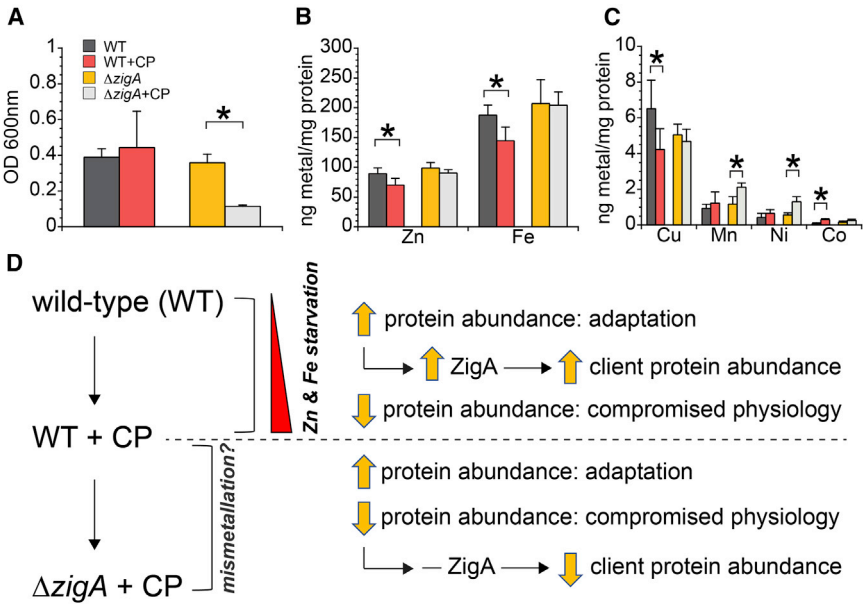

Figure 3. Calprotectin Induces Metal Starvation in *A. baumannii*

(A–C) Growth yield at 4 h (OD 600 nm) (A) of cell cultures treated with 0 or 200 μg/mL CP when cell samples were collected for determination of total cell-associated metal by inductively coupled plasma mass spectrometry (ICP-MS) (B and C). Total cell-associated metal of WT and Δ*zigA* cells is shown in (B) for zinc (Zn) and iron (Fe) and in (C) for other transition metals. The results shown reflect the mean of three independent replicates ±SD. *$p \leq 0.05$ as determined by Student's t test.

(D) Rationale and design of this study using Δ*zigA* as a tool to study the effects of extreme metal limitation.

See also Figure S3.

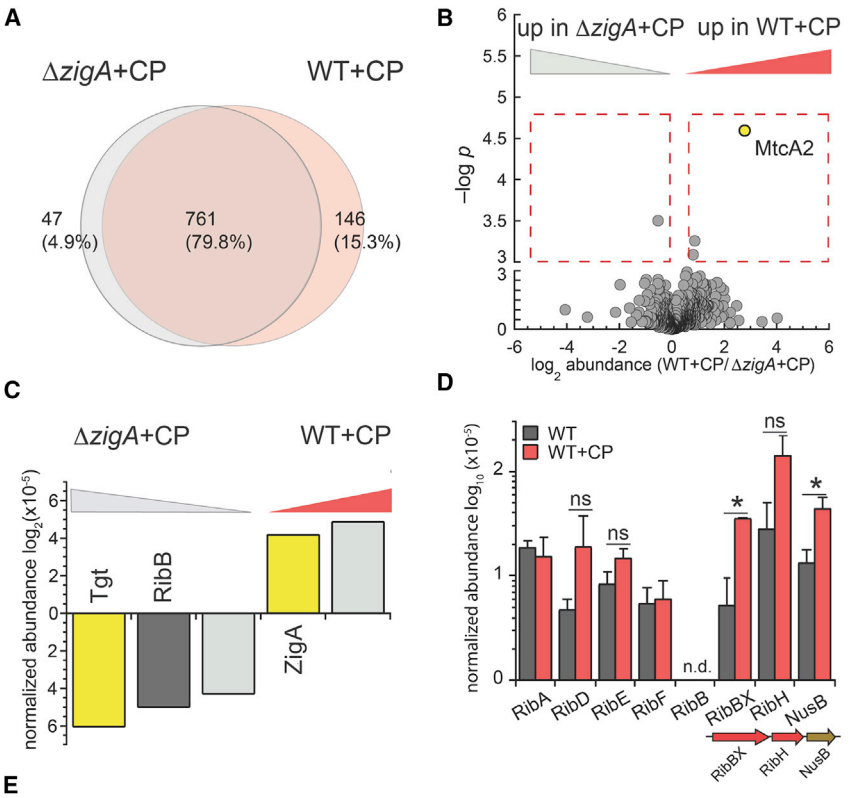

Figure 4. LC-MS/MS Proteomic Analysis for WT and Δ*zigA A. baumannii*

Protein profiles of WT (WT + CP) versus Δ*zigA* (Δ*zigA* + CP) *A. baumannii* cells treated with 200 μg/mL calprotectin from four biological replicates.

(A and B) (A) Venn diagram and (B) volcano plot for proteins detected at least three times under each condition in four replicates. The significance threshold was set at $p \leq 0.001$ and fold change in protein abundance at >1.3 as shown in the red dashed-line box. Yellow, Zn-binding proteins.

(C) Proteins that are strongly changed in WT + CP and Δ*zigA* + CP cells. Normalized protein abundance for proteins that were detected only in WT + CP or Δ*zigA* + CP for in all four replicates with the significance threshold set at the top-most 50% abundance (see Figures S2A and S2D).

(D) Normalized protein abundances of enzymes of the flavin biosynthetic (*rib*) pathway (compare with Figure S4F) in the WT (gray) or WT + CP (red) cells. *$p \leq 0.05$ as determined by Student's t test. Except for the RibF, which was detected only twice in four replicates in WT, all proteins shown were detected in at least three of the four biological replicates. The mean of independent replicates ±SD. is shown.

(E) Riboflavin biosynthesis pathway in *A. baumannii*. Metabolites are indicated in bold and Zn^{II} metalloenzymes are highlighted in blue.

See also Figure S4; Tables S4 and S5.

The increased cell abundance of RibBX induced by CP stress implies a functional role that is compensatory to RibB under CP stress (Figure 4E), although the function of RibBX is unknown. This is particularly true for the C-terminal RibX domain that is homologous to RibA, but appears to lack the Zn^{II} coordinating residues of authentic RibA. We measured the DHBPS and GCHII activity of RibBX (Figure 5) and found that RibBX possesses robust DHBPS activity that is comparable to that of authentic DHBPS (RibB) (Figure 5A), but is completely devoid of GCHII activity, consistent with the loss of all three cysteine ligands to the Zn (Singh et al., 2013) (Figure 5B). We then noted that purified RibBX solution is yellow, which suggests the presence of a bound flavin (Figure S5A); indeed, LC-MS/MS analysis revealed sub-stoichiometric FMN (Figure S5B). We then used FMN-stripped RibBX to show that FMN binds reversibly to RibBX, with a K_a of 1.4 ± 0.5 μM^{-1} and a subunit binding stoichiometry near 1:1 by isothermal titration calorimetry (ITC) (Figure 5C). We then reasoned that FMN might regulate the DHBPS activity of RibBX because in some organisms FMN regulates flavin biosynthesis through a canonical FMN-sensing riboswitch (Baird et al., 2010), which is predicted to fold upstream of *ribB* in *A. baumannii*, but not upstream of *ribBX*. To test this hypothesis, we measured the DHBPS activity of both RibBX and RibB in the presence of increasing FMN (Figures 5D and S5C), and only RibBX is inhibited by FMN, but with a K_i value of 7.8 μM (comparable to K_a). We note that this K_i is 3–4 orders of magnitude higher than observed for FMN riboswitch-mediated regulation of *ribB* in other bacteria.

To gain additional insight into the FMN-mediated inhibition of RibBX activity, we determined its structure by X-ray crystallography using molecular replacement with *Mtb* RibBA (Singh et al., 2013) (see Table S6 for structure statistics). *A. baumannii* RibBX crystallizes as a pseudo-D_2 symmetric homotetramer (Figure S5F). In solution, however, RibBX is a dimer and the oligomerization state is not significantly affected by the presence of bound FMN (Figure S5D). As anticipated, the overall architecture of RibBX is similar to that of *Mtb* RibBA, with a canonical RibB domain (Islam et al., 2015) (Figure 6A). The RibX domain adopts a topology highly similar to that of the GCHII (RibA) domain of *Mtb* RibBA, but with no Zn^{II} site present (Figure 6B). We hypothesized

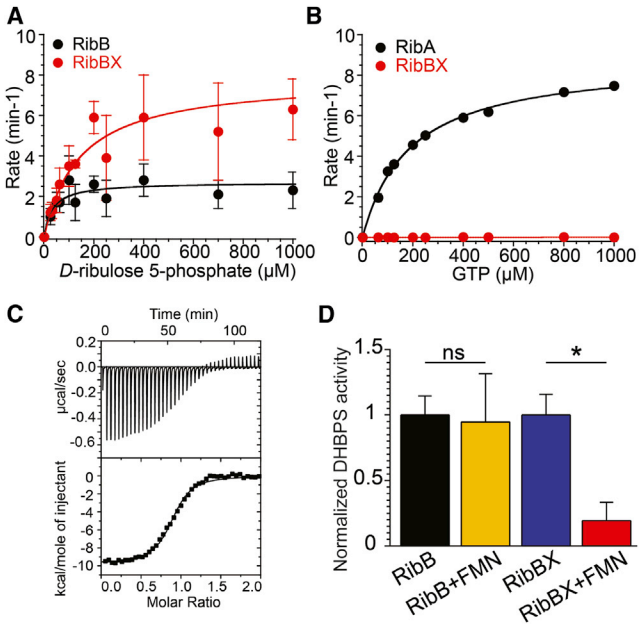

Figure 5. Biochemical Characterization of RibBX

(A) Michaelis-Menten plot for DHBPS activity with various substrate Ru5P concentrations. Error bars represent SD from three replicates. RibBX is in red. RibB (black) is the authentic DHBPS in *A. baumannii*.

(B) Michaelis Menten plot for GCHII activity with various substrate GTP concentrations. Error bars represent SD from three replicates. RibBX is in red. RibA (black) is the authentic GCHII in *A. baumannii*.

(C) Isothermal titration calorimetry (ITC) of FMN to RibBX. A representative fitting of three replicates is shown.

(D) Inhibition of DHBPS activity with 200 μM FMN. Reaction rate is normalized to the value with 0 μM FMN. *$p \leq 0.05$ using Student's t test. The mean of three independent replicates ±SD is shown.

See also Figure S5.

that FMN binds in RibX domain and allosterically regulates RibB-domain activity (see Figure S5G). These structural and functional findings suggest a dual regulatory model of flavin biosynthesis that is employed by cells experiencing transition metal perturbation (Figure 6C).

Flavin Supplementation Complements the Δ*zigA* Growth Phenotype

We hypothesized that in the dual regulatory model the cellular flavin supply is tightly regulated by balancing the activities and cell abundance of RibA, RibB, and RibBX. To elucidate the importance of *ribBX*, we found that a Δ*ribBX* strain has a significant growth defect during Zn starvation (Figure 7A). Given the differential abundance of RibBX in the WT and Δ*zigA* strains, the contribution of RibBX to the *A. baumannii* response to Zn limitation was interrogated in a system uncoupled from any transcriptional regulation that may exist for *ribBX*. *ribBX* was expressed under a constitutive promoter in WT and Δ*zigA A. baumannii*, and these strains were grown under Zn limitation induced by tetrakis-(2-pyridylmethyl)ethylenediamine (TPEN). Constitutive expression of *ribBX* did not alter the growth of WT or Δ*zigA* under Zn-replete conditions. However, under Zn-starved conditions, the Δ*zigA* strain experienced growth inhibition upon expression of *ribBX*, whereas *ribBX* expression improved growth in WT *A. baumannii* during Zn limitation (Figures 7B and S5E). These data reveal that RibBX helps overcome nutrient Zn limitation in *A. baumannii*.

Cellular Flavin Levels Are Markedly Lower in Δ*zigA* under CP Stress

The proteomics data suggest an impact on cellular flavin levels mediated by CP stress and/or ZigA (Figure 4D), as summarized in our dual regulatory model (Figure 6C). To test this, we quantified FAD levels as a proxy of flux through the riboflavin biosynthesis pathway. The Δ*zigA* strain has notably reduced total cellular FAD levels, but only under CP stress (Figure 7C), a finding consistent with the detection of RibB only in these cells, whose levels are predicted to be strongly repressed by a canonical FMN-sensing riboswitch under unstressed conditions (Serganov et al., 2009) (Figure 4C). Both CP-stressed (Figure 7C) and TPEN-treated (Figures S6A and S6B) Δ*zigA* cells show reduced flavin supply and induce a growth yield phenotype (Figures 3A and S5E); indeed, the Δ*ribBX* strain has lower levels of FAD even under Zn-replete conditions (Figure S6A).

Exogenous Flavin Partially Rescues the Growth Deficiency of Δ*zigA* under CP Stress

Our dual regulatory model predicts that supplementation of the Δ*zigA* strain with riboflavin might rescue this growth phenotype observed during CP- or TPEN-mediated metal limitation. To test this prediction, we employed a minimal growth medium with a carbon source that would increase the cellular demand for both flavins and Fe, and supplement with riboflavin, as riboflavin is the precursor to FMN and FAD (Figure 4E) (Nwugo et al., 2011). We used succinate and fumarate, two tricarboxylic acid cycle (TCA cycle) intermediates, for this purpose. Succinate dehydrogenase is a 4Fe-4S, flavin and heme-requiring enzyme that interconverts succinate and fumarate, while FumA is a 4Fe-4S cluster-containing enzyme that converts fumarate to malate and whose cellular levels are decreased in CP-stressed cells (Figure 2C). Both WT and the Δ*zigA* strain have similar growth kinetics in Zn-replete minimal medium with either succinate or fumarate as the sole carbon source, but not riboflavin under Zn-replete conditions (Figures S6C–S6E). Strikingly, under Zn-deplete conditions, the Δ*zigA* strain has a dramatic growth defect, which can be partially rescued by supplementation with low levels of riboflavin (Figures 7D, S6F, and S6G), but not by folate, the biosynthesis of which is also initiated from a Zn enzyme, GTP cyclohydrolase I (FolE) (Figures S7A and S7B). Neither WT or Δ*zigA A. baumannii* is able to utilize riboflavin as a carbon source, revealing that this growth rescue is not from additional carbon source supplementation (Figure S6C). Growth of Δ*zigA* and the effect of riboflavin supplementation under Zn-deplete conditions are not observed in a rich growth medium, revealing that increasing the cellular Fe requirement via the use of fumarate or succinate as the sole carbon source also exacerbates the demand for flavins (Figures S7C and S7D). Consistent with this prediction, both the Δ*zigA* and the Δ*ribBX* strains have significant growth defects compared with the WT strain when succinate is provided

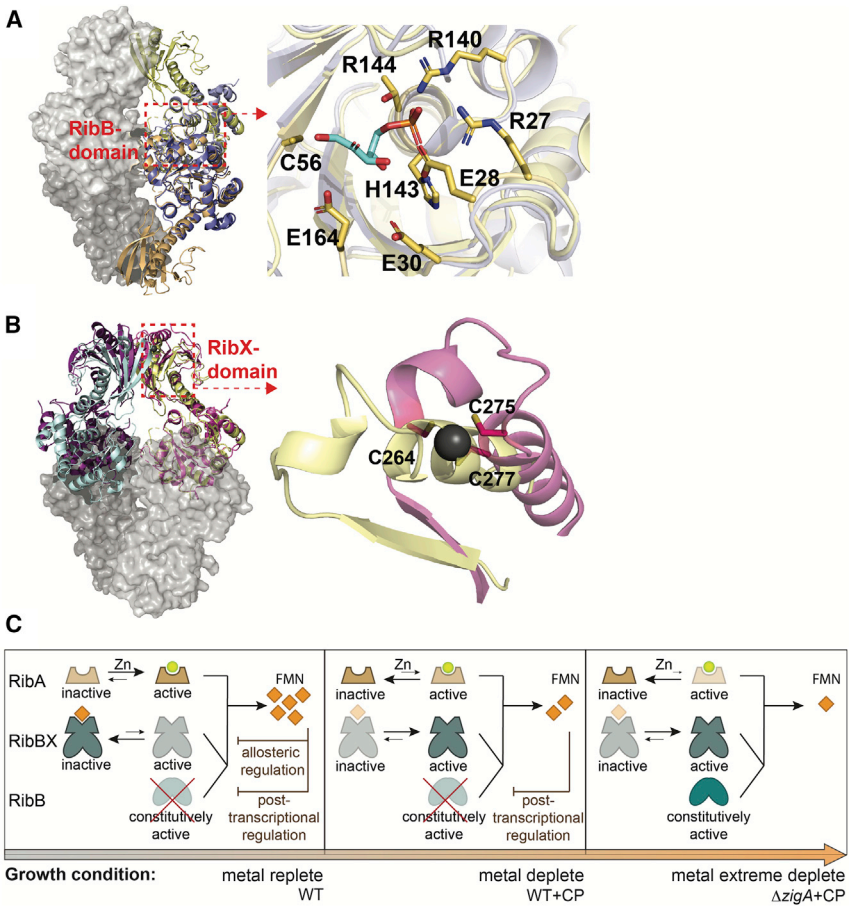

Figure 6. Crystal Structure of *A. baumannii* RibBX

(A) Superposition of structures of RibBX (bright orange and pale yellow) and *Vibrio cholerae* RibB (Islam et al., 2015) in the D-ribulose-5-phosphate-bound form (blue). Substrate binding residues are indicated for RibBX (bold).

(B) Superposition of structures of RibBX (pale cyan and pale yellow) and *Mycobacterium tuberculosis* RibBA (Singh et al., 2013) (*Mtb* RibBA; Rv1415) in the apo form (magenta). Zinc-binding residues in *Mtb* RibBA are shown (stick representation).

(C) Proposed dual regulatory model of the riboflavin biosynthesis pathway that becomes operative under extreme metal limitation mediated by CP.

See also Figure S5; Table S6.

as the sole carbon source and Fe is restricted by the Fe chelator ethylenediamine-di(*o*-hydroxyphenylacetic acid) (Figures S7E and S7F).

DISCUSSION

The findings presented here reveal a CP-induced multi-metal (Fe and Zn) perturbation of transition metal bioavailability that is exacerbated by the loss of ZigA in a way that has an impact on central metabolic processes in an important human pathogen. These processes include *de novo* flavin biosynthesis, the product of which functions as an essential cofactor involved in many aspects of cellular redox and energy metabolism (Bacher et al., 2000), and potentially other Zn-requiring enzymes, including the β-carbonic anhydrase (MtcA2) (Supuran and Capasso, 2017) and enzymes (QueD and Tgt) of the queuosine-tRNA biosynthesis pathway (McCarty and Bandarian, 2012). We describe a dual regulation model of flavin biosynthesis that is orchestrated by the DHBPS RibB and a unique, structurally characterized RibBX, which functions in an effort to maintain cellular flavin sufficiency under conditions of CP-induced metal starvation and the loss of ZigA. The fact that RibBX homologs are widespread in Proteobacteria (Brutinel et al., 2013) highlights the importance of this dual regulation model of flavin biosynthesis in other bacteria.

It is now well established that CP is a broad-spectrum chelator capable of inducing microenvironmental niche- and pathogen-dependent transition metal starvation (Zygiel et al., 2019; Zygiel and Nolan, 2018). The niche dependence is likely due to the spectrum of total metals defined by the site of infection (Cassat et al., 2018). However, it is often not clear how much of this total metal is bioavailable at infection sites, since the metal speciation in complex environments is not typically known (Juttukonda et al., 2017). As proxy for this, and from the perspective of comparing data obtained under different culture conditions, we have surveyed a sampling of typical growth media and found that the total metal composition and the ability of CP to deplete metals from these media vary dramatically (Figure S1). We conclude that although CP is clearly capable of depleting divalent metals, what metals CP depletes from the growth medium appears strongly influenced by the relative concentrations of total metal and total CP-binding sites. The coupling between the niche-dependent metal depletion by CP and intrinsic metal requirements in different bacteria (Lisher and Giedroc, 2013) potentially unifies previously conflicting responses to CP in various organisms.

Here, using a standard growth medium, we confirmed an adaptive response to Zn starvation regulated by Zur (Mortensen et al., 2014), but also revealed a strong Fe limitation response, in that siderophore biosynthesis and utilization genes are found to be notably upregulated at both the transcriptome and the proteome levels in *A. baumannii.* These findings are fully consistent with our metal analysis (Figure S1), and the previous observation that CP reduces Fe uptake in multiple bacteria (Zygiel et al., 2019). On one hand, Zn^{II} starvation may affect the functional integrity of the global Fe regulator Fur, since Fur contains a structural Zn^{II} site. On the other hand, CP induced a Zur-regulated putative stand-alone siderophore receptor protein (A1S_0092), which may have a unique role in transition metal acquisition and/or represent regulatory overlap between Zur and Fe limitation. Our findings also provide further evidence that transition

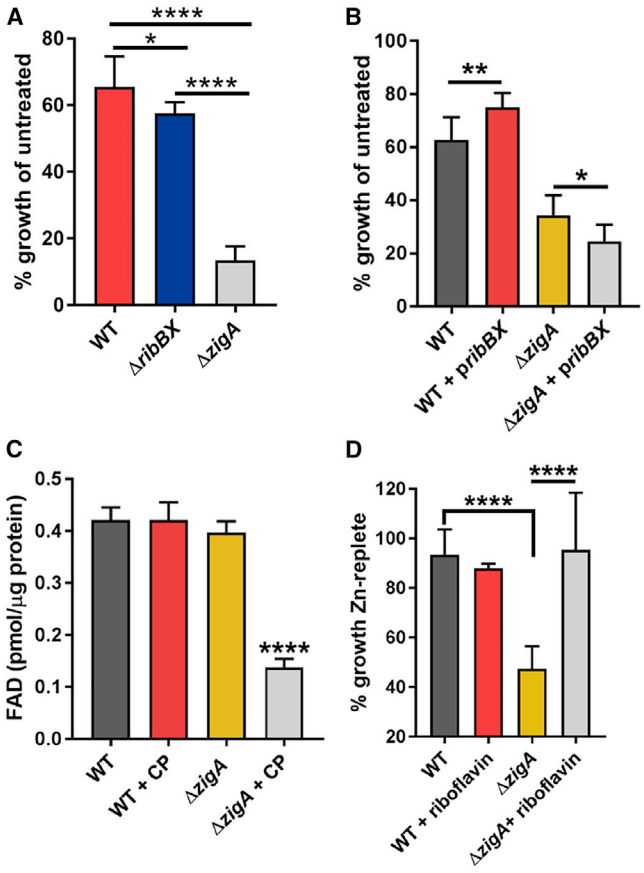

Figure 7. Riboflavin Can Rescue the Growth of Δ*zigA*

(A) Growth of Δ*ribBX* and Δ*zigA* is impaired with 40 μM TPEN. The mean of at least three independent replicates ±SD is shown.

(B) Constitutive expression of *ribBX* in the presence of 20 μM TPEN improves growth of WT *A. baumannii* but impairs growth of Δ*zigA*.

(C) Cellular FAD levels are notably decreased only in the Δ*zigA* strain in the presence of CP.

(D) Riboflavin partially rescues the growth phenotype of Δ*zigA* with fumarate as the sole carbon source in Zn-deplete conditions. See text for additional details. *$p \leq 0.05$, **$p \leq 0.01$, and ****$p < 0.0001$ as determined by one-way ANOVA with Tukey multiple comparisons test. The mean of at least three independent replicates ±SD is shown. See also Figures S5–S7.

metal homeostasis systems are interconnected (Hassan et al., 2017). Genes detected in RNA-seq involved in Fe metabolism are not differentially expressed in the Δ*zur* strain, demonstrating that their upregulation is mediated through a Zur-independent mechanism (Mortensen et al., 2014). The detection of a candidate cell-abundant Csp3 suggests that cytoplasmic Csp3 traps Cu^{I} (Dennison et al., 2018) and thus potentially allows *A. baumannii* to cope with the restricted bioavailability of Zn and Fe (Figure 3D); *A. baumannii* may also have an as-yet unknown nutritional need for Cu.

ZigA is a key player in response to Zn starvation and infection in mice, but how ZigA functions at the molecular level is unclear. ZigA exhibits weak GTPase activity and binds Zn^{II} with high affinity, and is therefore proposed to be a Zn metallochaperone from the COG0523 family (Nairn et al., 2016). As a result, the loss of ZigA may exacerbate cellular metal deficiency due to a failure to mobilize or allocate cellular Zn from metal complexes to high-priority protein targets that emerge under conditions of extreme metal limitation, with little or no impact on total metal. Regardless of the mechanism, we employed the Δ*zigA* strain as a tool to assess changes in the proteome that could be reporting on perturbations in metabolism that result from the loss of ZigA under these Zn/Fe-starved conditions. We identified two cellular processes, *de novo* flavin biosynthesis and queuosine-tRNA biosynthesis, that appear strongly affected by extreme CP-induced metal depletion.

It is known that in bacteria and plants, flavodoxins are required as non-metal substitutes for ferredoxins, thus prioritizing (ribo) flavin biosynthesis under these conditions (Pi and Helmann, 2017; Sepulveda Cisternas et al., 2018; Tognetti et al., 2007). In *Helicobacter pylori*, riboflavin is reported to be secreted from cells and is thought to participate in Fe reduction to Fe^{II} and acquisition potentially through FeoAB (Figure 1B), with the flavin biosynthesis pathway found to be upregulated under Fe deficiency (Worst et al., 1998); this is true in other bacteria as well (da Silva Neto et al., 2013; Vasileva et al., 2012). Recent work reveals that riboflavin and Fe levels are reciprocally regulated in *Vibrio cholerae* (Sepulveda-Cisternas et al., 2018), and we observe elements of this in *A. baumannii*, since the Δ*ribBX* strain, like the Δ*zigA* strain, is sensitive to Fe starvation (Figures S7E and S7F). Although in *Bacillus subtilis*, *ribBA* expression is reported to be Fur regulated (Worst et al., 1998), it is unknown how the transcription of the *ribBX* operon is regulated in *A. baumannii*. We showed here that while RibBX has WT-like DHBPS activity under conditions where authentic RibB is not detected in cells, RibBX is subjected to product inhibition by cellular FMN, but only at very high concentrations, and thus can be used in CP-treated cells to bypass the regulatory control of the FMN-sensing riboswitch upstream of *ribB* under these conditions (Figure 6C) (Serganov et al., 2009). We also found that two enzymes, QueD and Tgt, also become more cell abundant in CP-stressed cells, thus suggesting that queuosine-tRNA biosynthesis, a second pathway downstream of FolE, is prioritized under these conditions. The cellular logic for this is unknown, but this tRNA modification is strongly implicated as involved in response to CP-induced metal starvation in *A. baumannii*.

In summary, we show here that CP treatment of *A. baumannii* under these growth conditions strongly restricts the availability of Zn and Fe. The bacteria respond by inducing an acute cellular response to Zn and Fe deficiency while limiting the bioavailability of Cu. CP stress affects flavin biosynthesis, and it is plausible that Fe homeostasis and flavin biosynthesis are reciprocally regulated in *A. baumannii*. Taken together, these results outline significant cross talk between metal homeostasis systems and a key intersection with flavin, and perhaps queuosine, biosynthetic pathways. These results also identify cell-abundant antimicrobial targets, including MtcA2 (Aspatwar et al., 2018; Supuran and Capasso, 2017), DapE (Gillner et al., 2013; Starus et al., 2015), ZigA, and RibBX, for the development of antibacterial strategies for the treatment of *A. baumannii* infection while this multi-drug-resistant organism is actively subjected to nutritional immunity in the infected host.

SIGNIFICANCE

Vertebrate host-derived nutritional immunity, defined as transition metal withholding, and transition metal toxicity operate at the host-microbial pathogen interface in an effort to limit the impact of bacterial infections. Calprotectin (CP) is one of a large family of Ca^{II}-activated transition metal-binding proteins, secreted by neutrophils that migrate to sites of infection, to starve those bacteria of these essential metals. Although CP is a versatile transition metal chelator, significant questions remain as to what metals are sequestered by CP at infection sites and how the loss of specific metals affects cellular physiology. Here, we show that CP induces an acute Zn^{II} and Fe starvation response in the important opportunistic pathogen *Acinetobacter baumannii*, and probe the function of the Zn-uptake repressor (Zur)-regulated GTPase ZigA in cellular adaptation to CP. We show that CP and the loss of ZigA severely lowers cellular flavin levels, and that a major metabolic response to CP-mediated Fe restriction is a prioritization of *de novo* flavin biosynthesis. We uncover a dual regulatory model of (ribo)flavin biosynthesis that is operative under these metal-deplete conditions and present the crystallographic structure of a fusion protein, RibBX, which is feedback inhibited by flavin mononucleotide but only at high intracellular flavin. This work investigates the cellular mechanisms of adaption to Fe starvation as key feature of CP-induced cellular stress, and further refines our understanding of the intersection of metal homeostasis systems and the flavin biosynthesis pathway in an important human pathogen. Further, in addition to the proteins ZigA and RibBX, we identify a number of Zn metalloenzymes that are established antimicrobial targets and are cell abundant under conditions of host-derived nutritional immunity, which might be leveraged for the development of antimicrobial strategies against *A. baumannii.*

STAR★METHODS

Detailed methods are provided in the online version of this paper and include the following:

- KEY RESOURCES TABLE
- CONTACT FOR REAGENT AND RESOURCE SHARING
- EXPERIMENTAL MODEL AND SUBJECT DETAILS
  - Bacterial Strains and Reagents
- METHODS DETAILS
  - *A. baumannii* Mutant Generation
  - *A. baumannii* Expression Construct Generation
  - Growth in Calprotectin or Metal Chelators
  - ICP-MS Quantification of Total Metals
  - RNA Sequencing
  - Transcriptomic Analysis
  - Quantitative RT-PCR
  - LC-MS/MS Proteomic Analysis
  - Statistical Rationale and Bioinformatics Analysis
  - Siderophore Quantification
  - Zinc Proteome Prediction of *A. baumannii*
  - FAD Quantification
  - Purification of *A. baumannii* Proteins
  - GCHII Activity Assay
  - DHBPS Activity Assay
  - FMN Binding by ITC
  - Crystal Structure of RibBX
  - Analytical Gel Filtration Chromatography
  - *A. baumannii* Growth with Riboflavin
- QUANTIFICATION AND STATISTICAL ANALYSIS
- DATA AND SOFTWARE AVAILABILITY

SUPPLEMENTAL INFORMATION

Supplemental Information can be found online at https://doi.org/10.1016/j.chembiol.2019.02.011.

ACKNOWLEDGMENTS

The authors thank Dr. Daiana Capdevila and other members of the Giedroc and Skaar laboratories for their editorial comments on the manuscript. This research used resources of the Advanced Light Source, which is a Department of Energy Office of Science User Facility under contract DE-AC02-05CH11231. We thank Jay Nix for his assistance during X-ray data collection in beamline 4.2.2. Work presented in this article was supported by grant R01 AI101171 to E.P.S., W.J.C., and D.P.G. and by R35 GM118157 to D.P.G. from the National Institutes of Health (NIH). Z.R.L. is supported by NIH F31 AI136255 and NIH T32 ES007028. The content of this article does not necessarily represent the views of the NIH and is solely the responsibility of the authors.

AUTHOR CONTRIBUTIONS

D.P.G., E.P.S., J.W., and Z.R.L. conceptualized and designed the study. J.W., Z.R.L., E.P.S., and D.P.G. wrote the manuscript. C.N.M. and W.J.C. generated and provided recombinant WT CP. B.L.N. performed the RNA-seq experiment. J.W. and Y.Z. performed the proteomics experiments under the supervision of J.C.T. C.A. performed the Zn proteome prediction. J.W. and G.G.G. performed the crystallography experiments. J.W. and Z.R.L. performed the growth experiments and all other remaining experiments. All authors provided feedback on the manuscript.

DECLARATION OF INTERESTS

The authors declare no competing interests.

Received: November 30, 2018
Revised: January 20, 2019
Accepted: February 18, 2019
Published: March 21, 2019

REFERENCES

Adams, P.D., Afonine, P.V., Bunkoczi, G., Chen, V.B., Davis, I.W., Echols, N., Headd, J.J., Hung, L.W., Kapral, G.J., Grosse-Kunstleve, R.W., et al. (2010). PHENIX: a comprehensive Python-based system for macromolecular structure solution. Acta Crystallogr. D Biol. Crystallogr. *66*, 213–221.

Alexander, D.B., and Zuberer, D.A. (1991). Use of chrome azurol-S reagents to evaluate siderophore production by Rhizosphere bacteria. Biol. Fertil. Soils *12*, 39–45.

Anders, S., and Huber, W. (2010). Differential expression analysis for sequence count data. Genome Biol. *11*, R106.

Andreini, C., Banci, L., Bertini, I., and Rosato, A. (2006). Zinc through the three domains of life. J. Proteome Res. *5*, 3173–3178.

Aspatwar, A., Winum, J.Y., Carta, F., Supuran, C.T., Hammaren, M., Parikka, M., and Parkkila, S. (2018). Carbonic anhydrase inhibitors as novel drugs

against mycobacterial beta-carbonic anhydrases: an update on *in vitro* and *in vivo* studies. Molecules *23*, 2911.

Bacher, A., Eberhardt, S., Fischer, M., Kis, K., and Richter, G. (2000). Biosynthesis of vitamin b2 (riboflavin). Annu. Rev. Nutr. *20*, 153–167.

Baird, N.J., Kulshina, N., and Ferre-D'Amare, A.R. (2010). Riboswitch function: flipping the switch or tuning the dimmer? RNA Biol. *7*, 328–332.

Besold, A.N., Gilston, B.A., Radin, J.N., Ramsoomair, C., Culbertson, E.M., Li, C.X., Cormack, B.P., Chazin, W.J., Kehl-Fie, T.E., and Culotta, V.C. (2017). The role of calprotectin in withholding zinc and copper from *Candida albicans*. Infect. Immun. *82*, e00779–00717.

Brutinel, E.D., Dean, A.M., and Gralnick, J.A. (2013). Description of a riboflavin biosynthetic gene variant prevalent in the phylum Proteobacteria. J. Bacteriol. *195*, 5479–5486.

Cassat, J.E., Moore, J.L., Wilson, K.J., Stark, Z., Prentice, B.M., Van de Plas, R., Perry, W.J., Zhang, Y., Virostko, J., Colvin, D.C., et al. (2018). Integrated molecular imaging reveals tissue heterogeneity driving host-pathogen interactions. Sci. Transl. Med. *10*, eaan6361.

Chen, V.B., Arendall, W.B., 3rd, Headd, J.J., Keedy, D.A., Immormino, R.M., Kapral, G.J., Murray, L.W., Richardson, J.S., and Richardson, D.C. (2010). MolProbity: all-atom structure validation for macromolecular crystallography. Acta Crystallogr. D Biol. Crystallogr. *66*, 12–21.

Clohessy, P.A., and Golden, B.E. (1995). Calprotectin-mediated zinc chelation as a biostatic mechanism in host defence. Scand. J. Immunol. *42*, 551–556.

Corbin, B.D., Seeley, E.H., Raab, A., Feldmann, J., Miller, M.R., Torres, V.J., Anderson, K.L., Dattilo, B.M., Dunman, P.M., Gerads, R., et al. (2008). Metal chelation and inhibition of bacterial growth in tissue abscesses. Science *319*, 962–965.

da Silva Neto, J.F., Lourenco, R.F., and Marques, M.V. (2013). Global transcriptional response of *Caulobacter crescentus* to iron availability. BMC Genomics *14*, 549.

Damo, S.M., Kehl-Fie, T.E., Sugitani, N., Holt, M.E., Rathi, S., Murphy, W.J., Zhang, Y.F., Betz, C., Hench, L., Fritz, G., et al. (2013). Molecular basis for manganese sequestration by calprotectin and roles in the innate immune response to invading bacterial pathogens. Proc. Natl. Acad. Sci. U S A *110*, 3841–3846.

Dennison, C., David, S., and Lee, J. (2018). Bacterial copper storage proteins. J. Biol. Chem. *293*, 4616–4627.

Doyle, J.S., Buising, K.L., Thursky, K.A., Worth, L.J., and Richards, M.J. (2011). Epidemiology of infections acquired in intensive care units. Semin. Respir. Crit. Care Med. *32*, 115–138.

Eddy, S.R. (1998). Profile hidden Markov models. Bioinformatics *14*, 755–763.

Emsley, P., Lohkamp, B., Scott, W.G., and Cowtan, K. (2010). Features and development of Coot. Acta Crystallogr. D Biol. Crystallogr. *66*, 486–501.

Finn, R.D., Bateman, A., Clements, J., Coggill, P., Eberhardt, R.Y., Eddy, S.R., Heger, A., Hetherington, K., Holm, L., Mistry, J., et al. (2014). Pfam: the protein families database. Nucleic Acids Res. *42*, D222–D230.

Gibson, D.G., Young, L., Chuang, R.Y., Venter, J.C., Hutchison, C.A., 3rd, and Smith, H.O. (2009). Enzymatic assembly of DNA molecules up to several hundred kilobases. Nat. Methods *6*, 343–345.

Gillner, D.M., Becker, D.P., and Holz, R.C. (2013). Lysine biosynthesis in bacteria: a metallodesuccinylase as a potential antimicrobial target. J. Biol. Inorg. Chem. *18*, 155–163.

Grossoehme, N.E., and Giedroc, D.P. (2009). Energetics of allosteric negative coupling in the zinc sensor *S. aureus* CzrA. J. Am. Chem. Soc. *131*, 17860–17870.

Harding, C.M., Hennon, S.W., and Feldman, M.F. (2018). Uncovering the mechanisms of *Acinetobacter baumannii* virulence. Nat. Rev. Microbiol. *16*, 91–102.

Hassan, K.A., Pederick, V.G., Elbourne, L.D., Paulsen, I.T., Paton, J.C., McDevitt, C.A., and Eijkelkamp, B.A. (2017). Zinc stress induces copper depletion in *Acinetobacter baumannii*. BMC Microbiol. *17*, 59.

Hoang, T.T., Karkhoff-Schweizer, R.R., Kutchma, A.J., and Schweizer, H.P. (1998). A broad-host-range Flp-FRT recombination system for site-specific excision of chromosomally-located DNA sequences: application for isolation of unmarked *Pseudomonas aeruginosa* mutants. Gene *212*, 77–86.

Hood, M.I., Mortensen, B.L., Moore, J.L., Zhang, Y., Kehl-Fie, T.E., Sugitani, N., Chazin, W.J., Caprioli, R.M., and Skaar, E.P. (2012). Identification of an *Acinetobacter baumannii* zinc acquisition system that facilitates resistance to calprotectin-mediated zinc sequestration. PLoS Pathog. *8*, e1003068.

Hood, M.I., and Skaar, E.P. (2012). Nutritional immunity: transition metals at the pathogen-host interface. Nat. Rev. Microbiol. *10*, 525–537.

Islam, Z., Kumar, A., Singh, S., Salmon, L., and Karthikeyan, S. (2015). Structural basis for competitive inhibition of 3,4-dihydroxy-2-butanone-4-phosphate synthase from *Vibrio cholerae*. J. Biol. Chem. *290*, 11293–11308.

Jacobsen, F.E., Kazmierczak, K.M., Lisher, J.P., Winkler, M.E., and Giedroc, D.P. (2011). Interplay between manganese and zinc homeostasis in the human pathogen *Streptococcus pneumoniae*. Metallomics *3*, 38–41.

Juttukonda, L.J., Berends, E.T.M., Zackular, J.P., Moore, J.L., Stier, M.T., Zhang, Y., Schmitz, J.E., Beavers, W.N., Wijers, C.D., Gilston, B.A., et al. (2017). Dietary manganese promotes Staphylococcal infection of the heart. Cell Host Microbe *22*, 531–542.e8.

Kabsch, W. (2010). Integration, scaling, space-group assignment and post-refinement. Acta Crystallogr. D Biol. Crystallogr. *66*, 133–144.

Kentache, T., Ben Abdelkrim, A., Jouenne, T., De, E., and Hardouin, J. (2017). Global dynamic proteome study of a pellicle-forming *Acinetobacter baumanni*i strain. Mol. Cell Proteomics *16*, 100–112.

Langmead, B., and Salzberg, S.L. (2012). Fast gapped-read alignment with Bowtie 2. Nat. Methods *9*, 357–359.

LaRoche, J., Boyd, P.W., McKay, R.M.L., and Geider, R.J. (1996). Flavodoxin as an *in situ* marker for iron stress in phytoplankton. Nature *382*, 802–805.

Lee, J.W., and Helmann, J.D. (2007). Functional specialization within the Fur family of metalloregulators. Biometals *20*, 485–499.

Lisher, J.P., and Giedroc, D.P. (2013). Manganese acquisition and homeostasis at the host-pathogen interface. Front. Cell. Infect. Microbiol. *3*, 91.

Magoc, T., Wood, D., and Salzberg, S.L. (2013). EDGE-pro: estimated degree of gene expression in prokaryotic genomes. Evol. Bioinform. Online *9*, 127–136.

McCarty, R.M., and Bandarian, V. (2012). Biosynthesis of pyrrolopyrimidines. Bioorg. Chem. *43*, 15–25.

Menard, R., Sansonetti, P.J., and Parsot, C. (1993). Nonpolar mutagenesis of the *Ipa* genes defines Ipab, Ipac, and Ipad as effectors of *Shigella flexneri* entry into epithelial cells. J. Bacteriol. *175*, 5899–5906.

Mortensen, B.L., Rathi, S., Chazin, W.J., and Skaar, E.P. (2014). *Acinetobacter baumannii* response to host-mediated zinc limitation requires the transcriptional regulator Zur. J. Bacteriol. *196*, 2616–2626.

Nairn, B.L., Lonergan, Z.R., Wang, J., Braymer, J.J., Zhang, Y., Calcutt, M.W., Lisher, J.P., Gilston, B.A., Chazin, W.J., de Crecy-Lagard, V., et al. (2016). The response of *Acinetobacter baumannii* to zinc starvation. Cell Host Microbe *19*, 826–836.

Nakashige, T.G., Zhang, B., Krebs, C., and Nolan, E.M. (2015). Human calprotectin is an iron-sequestering host-defense protein. Nat. Chem. Biol. *11*, 765–771.

Nakashige, T.G., Zygiel, E.M., Drennan, C.L., and Nolan, E.M. (2017). Nickel sequestration by the host-defense protein human calprotectin. J. Am. Chem. Soc. *139*, 8828–8836.

Nwugo, C.C., Gaddy, J.A., Zimbler, D.L., and Actis, L.A. (2011). Deciphering the iron response in *Acinetobacter baumannii*: a proteomics approach. J. Proteomics *74*, 44–58.

Overbeek, R., Begley, T., Butler, R.M., Choudhuri, J.V., Chuang, H.Y., Cohoon, M., de Crecy-Lagard, V., Diaz, N., Disz, T., Edwards, R., et al. (2005). The subsystems approach to genome annotation and its use in the project to annotate 1000 genomes. Nucleic Acids Res. *33*, 5691–5702.

Park, A.J., Murphy, K., Krieger, J.R., Brewer, D., Taylor, P., Habash, M., and Khursigara, C.M. (2014). A temporal examination of the planktonic and biofilm proteome of whole cell *Pseudomonas aeruginosa* PAO1 using quantitative mass spectrometry. Mol. Cell. Proteomics *13*, 1095–1105.

Phillips, G., Grochowski, L.L., Bonnett, S., Xu, H., Bailly, M., Blaby-Haas, C., El Yacoubi, B., Iwata-Reuyl, D., White, R.H., and de Crecy-Lagard, V. (2012). Functional promiscuity of the COG0720 family. ACS Chem. Biol. *7*, 197–209.

Pi, H., and Helmann, J.D. (2017). Sequential induction of Fur-regulated genes in response to iron limitation in *Bacillus subtilis*. Proc. Natl. Acad. Sci. U S A *114*, 12785–12790.

Putignano, V., Rosato, A., Banci, L., and Andreini, C. (2018). MetalPDB in 2018: a database of metal sites in biological macromolecular structures. Nucleic Acids Res. *46*, D459–D464.

Rosato, A., Valasatava, Y., and Andreini, C. (2016). Minimal functional sites in metalloproteins and their usage in structural bioinformatics. Int. J. Mol. Sci. *17*, 671.

Schwyn, B., and Neilands, J.B. (1987). Universal chemical assay for the detection and determination of siderophores. Anal. Biochem. *160*, 47–56.

Sepulveda Cisternas, I., Salazar, J.C., and Garcia-Angulo, V.A. (2018). Overview on the bacterial iron-riboflavin metabolic axis. Front. Microbiol. *9*, 1478.

Sepulveda-Cisternas, I., Lozano Aguirre, L., Fuentes Flores, A., Vasquez Solis de Ovando, I., and Garcia-Angulo, V.A. (2018). Transcriptomics reveals a cross-modulatory effect between riboflavin and iron and outlines responses to riboflavin biosynthesis and uptake in *Vibrio cholerae*. Sci. Rep. *8*, 3149.

Serganov, A., Huang, L., and Patel, D.J. (2009). Coenzyme recognition and gene regulation by a flavin mononucleotide riboswitch. Nature *458*, 233–237.

Sheffield, P., Garrard, S., and Derewenda, Z. (1999). Overcoming expression and purification problems of RhoGDI using a family of "parallel" expression vectors. Protein Expr. Purif. *15*, 34–39.

Singh, M., Kumar, P., Yadav, S., Gautam, R., Sharma, N., and Karthikeyan, S. (2013). The crystal structure reveals the molecular mechanism of bifunctional 3,4-dihydroxy-2-butanone 4-phosphate synthase/GTP cyclohydrolase II (Rv1415) from *Mycobacterium tuberculosis*. Acta Crystallogr. D Biol. Crystallogr. *69*, 1633–1644.

Starus, A., Nocek, B., Bennett, B., Larrabee, J.A., Shaw, D.L., Sae-Lee, W., Russo, M.T., Gillner, D.M., Makowska-Grzyska, M., Joachimiak, A., et al. (2015). Inhibition of the *dapE*-encoded N-succinyl-L,L-diaminopimelic acid desuccinylase from *Neisseria meningitidis* by L-Captopril. Biochemistry *54*, 4834–4844.

Straw, M.L., Chaplin, A.K., Hough, M.A., Paps, J., Bavro, V.N., Wilson, M.T., Vijgenboom, E., and Worrall, J.A.R. (2018). A cytosolic copper storage protein provides a second level of copper tolerance in *Streptomyces lividans*. Metallomics *10*, 180–193.

Supuran, C.T., and Capasso, C. (2017). An overview of the bacterial carbonic anhydrases. Metabolites *7*, 56.

Tognetti, V.B., Zurbriggen, M.D., Morandi, E.N., Fillat, M.F., Valle, E.M., Hajirezaei, M.R., and Carrillo, N. (2007). Enhanced plant tolerance to iron starvation by functional substitution of chloroplast ferredoxin with a bacterial flavodoxin. Proc. Natl. Acad. Sci. U S A *104*, 11495–11500.

UniProt Consortium, T (2018). UniProt: the universal protein knowledgebase. Nucleic Acids Res. *46*, 2699.

Valasatava, Y., Rosato, A., Banci, L., and Andreini, C. (2016). MetalPredator: a web server to predict iron-sulfur cluster binding proteomes. Bioinformatics *32*, 2850–2852.

Vasileva, D., Janssen, H., Honicke, D., Ehrenreich, A., and Bahl, H. (2012). Effect of iron limitation and *fur* gene inactivation on the transcriptional profile of the strict anaerobe *Clostridium acetobutylicum*. Microbiology *158*, 1918–1929.

Vinayak, M., and Pathak, C. (2010). Queuosine modification of tRNA: its divergent role in cellular machinery. Biosci. Rep. *30*, 135–148.

Wakeman, C.A., Moore, J.L., Noto, M.J., Zhang, Y., Singleton, M.D., Prentice, B.M., Gilston, B.A., Doster, R.S., Gaddy, J.A., Chazin, W.J., et al. (2016). The innate immune protein calprotectin promotes *Pseudomonas aeruginosa* and *Staphylococcus aureus* interaction. Nat. Commun. *7*, 11951.

Wang, L., Wang, S., and Li, W. (2012). RSeQC: quality control of RNA-seq experiments. Bioinformatics *28*, 2184–2185.

Weinberg, E.D. (1975). Nutritional immunity: Host's attempt to withhold iron from microbial invaders. JAMA *231*, 39–41.

Worst, D.J., Gerrits, M.M., Vandenbroucke-Grauls, C.M., and Kusters, J.G. (1998). *Helicobacter pylori* ribBA-mediated riboflavin production is involved in iron acquisition. J. Bacteriol. *180*, 1473–1479.

Yoneyama, H., and Nakae, T. (1996). Protein C (OprC) of the outer membrane of *Pseudomonas aeruginosa* is a copper-regulated channel protein. Microbiology *142*, 2137–2144.

Zygiel, E.M., Nelson, C.E., Brewer, L.K., Oglesby-Sherrouse, A.G., and Nolan, E.M. (2019). The human innate immune protein calprotectin induces iron starvation responses in *Pseudomonas aeruginosa*. J. Biol. Chem. https://doi.org/10.1074/jbc.RA118.006819.

Zygiel, E.M., and Nolan, E.M. (2018). Transition metal sequestration by the host-defense protein calprotectin. Annu. Rev. Biochem. *87*, 621–643.

STAR★METHODS

KEY RESOURCES TABLE

REAGENT or RESOURCE	SOURCE	IDENTIFIER
Bacterial and Virus Strains		
E.coli: F$^-$ *ompT hsdS*$_B$ ($r_B^-m_B^-$) *gal dcm* (DE3)	Thermo Fisher Scientific	*E.coli* BL21(DE3)
E.coli: F$^-$ *ompT hsdS*$_B$ ($r_B^-m_B^-$) *gal dcm* (DE3)	Sigma	*E.coli* C41 (DE3)
E.coli: F$^-$ φ80*lac*ZΔM15 Δ(*lac*ZYA-*arg*F)U169 *rec*A1 *end*A1 *hsd*R17(r_k^-, m_k^+) *pho*A *sup*E44 *thi*-1 *gyr*A96 *rel*A1 λ$^-$	Thermo Fisher Scientific	*E.coli* DH5α
A. baumannii: ATCC 17978	ATCC	*A. baumannii* WT
A. baumannii: ATCC 17978 *ΔzigA*	(Nairn et al., 2016)	*ΔzigA*
A. baumannii: ATCC 17978 *ΔribBX*	This paper	*ΔribBX*
Chemicals, Peptides, and Recombinant Proteins		
Guanosine 5′-triphosphate (sodium salt hydrate)	Sigma	CAT# G8877
Riboflavin	Sigma	CAT# R7649-25G
Flavin mononucleotide (sodium salt hydrate)	Cayman	CAT# 18167
RNeasy preparation kit	Qiagen	CAT# 74104
RNase inhibitor	Thermo Fisher Scientific	CAT# EO0382
The Ribo-Zero rRNA removal kit for Gram-negative bacteria	Epicentre/Illumina	CAT# MRZGN126
TruSeq stranded mRNA sample preparation kit	Illumina	CAT# 20020595
Chrome azurol S	Sigma	CAT# 199532-25G
FAD assay kit	Abcam	CAT# ab204710
BCA assay	Thermo Fisher Scientific	CAT# 23225
D-ribulose-5-phosphate (sodium salt)	Cayman	CAT# 21423
Creatine monohydrate	Thermo Fisher Scientific	CAT# C3630
1-Naphthol	Sigma	CAT# N1000
MemGold2^{TM}	Molecular Dimensions	CAT# MD1-63
Gel Filtration Calibration Kit HMW	GE Healthcare	CAT# 28-4038-42
Sodium succinate dibasic hexahydrate	Sigma	CAT# S2378-500G
Sodium fumarate dibasic	Sigma	CAT# F1506-25G
RibA	This paper	N/A
RibB	This paper	N/A
RibBX	This paper	N/A
Deposited Data		
Structure of *A. baumannii* RibBX	This paper	PDB: 6MNZ
Structure of *M. tuberculosis* RibBA	(Singh et al., 2013)	PDB: 4I14
Structure of *V. cholerae* RibB	(Islam et al., 2015)	PDB: 4P8E
WT *A. baumannii* Zur RNASeq	(Mortensen et al., 2014)	N/A
Calprotectin *A. baumannii* RNASeq	This paper	GEO: GSE125491
Oligonucleotides		
Table S7	This paper	N/A
Recombinant DNA		
pHIS	(Sheffield et al., 1999)	pHIS
pHIS-*ribA*	This paper	N/A
pHIS-*ribB*	This paper	N/A
pHIS-*ribRX*	This paper	N/A

(*Continued on next page*)

Continued

REAGENT or RESOURCE	SOURCE	IDENTIFIER
pWH1266	ATCC	pWH1266
pWH1266-*ribRX*	This paper	N/A
Software and Algorithms		
CASAVA-1.8.2		https://bioweb.pasteur.fr/packages/pack@casava@1.8.2
EDGE-pro version 1.3	(Magoc et al., 2013)	N/A
Bowtie2 version 2.1.0	(Langmead and Salzberg, 2012)	N/A
DESeq	(Anders and Huber, 2010)	N/A
R-3.0.0		http://www.r-project.org
XDS	(Kabsch, 2010)	http://xds.mpimf-heidelberg.mpg.de
Xcaliber v4.0		https://www.thermofisher.com/order/catalog/product/OPTON-30487
Coot	(Emsley et al., 2010)	https://www2.mrc-lmb.cam.ac.uk/personal/pemsley/coot/
PHENIX	(Adams et al., 2010)	https://www.phenix-online.org/download/
MolProbity	(Chen et al., 2010)	http://molprobity.biochem.duke.edu

CONTACT FOR REAGENT AND RESOURCE SHARING

Further information and requests for materials should be directed to and fulfilled by the Lead Contact, David Giedroc (giedroc@indiana.edu) and Eric Skaar (eric.skaar@vanderbilt.edu).

EXPERIMENTAL MODEL AND SUBJECT DETAILS

Bacterial Strains and Reagents

Experiments were performed on *A. baumannii* ATCC 17978 and mutant derivatives of this strain, including the Δ*zigA* mutant generated previously (Nairn et al., 2016) and the Δ*ribBX* mutant generated as described below. Cloning was performed in *E. coli* DH5α and protein expression in *E. coli* BL21 (DE3). Strains were cultured in Luria Broth (LB) at 37°C with aeration unless otherwise noted, and OD_{600} was used to measure bacterial growth as previously described (Nairn et al., 2016). Kanamycin (Sigma) was used at 40 μg/mL. Ampicillin (Sigma) was used at 100 μg/mL for *E. coli* and 500 μg/mL for *A. baumannii*. Recombinant human CP were expressed and purified as previously described (Corbin et al., 2008). S100A8 and S100A9 cloned into pET1120 were transformed separately into *E. coli* C41 (DE3) cells for expression. Cells were induced at 37°C at OD_{600} between 0.6 and 0.8 with the addition of 1 mM isopropyl thio-β-D-galactoside (IPTG) and allowed to grow 4 hours post-induction. Cells were harvested by centrifugation (6500 rpm, 20 min, 4°C), and re-suspended in Lysis Buffer (50 mM Tris pH 8.0, 100 mM NaCl, 1 mM EDTA, 1 mM phenylmethane sulfonyl fluoride (PMSF), 0.5 % Triton X-100). Once homogenized, sample was sonicated (10 min, 50 watts, 5 s on/10 s off), and centrifuged (20,000 rpm, 20 min). The supernatant was filtered and loaded onto a SourceQ column (General Electric) with flow rate at 1 mL/min. After loading, the column was washed with three column volume (CV) Buffer A (20 mM Tris, pH 8.0) and eluted with a gradient from 0 to 100% Buffer B (20 mM Tris, pH 8.0, 1 M NaCl) over 10 CV. S100A8/A9 containing fractions were pooled according to SDS-PAGE, concentrated, and loaded onto S75 column (General Electric). The column was washed with 1 CV S75 Buffer (20 mM Tris, pH 8.0, 100 mM NaCl), S100A8/A9 containing fractions pooled according to SDS-PAGE, flash frozen, and stored at –80°C.

METHODS DETAILS

A. baumannii Mutant Generation

To generate in-frame the Δ*ribBX* strain, approximately 1000 base pairs of DNA in both the 5' and 3' flanking regions surrounding the open reading frame, leaving the N-terminal ~200 nucleotides of *ribBX* intact to limit polarity, were amplified from *A. baumannii* genomic DNA using primers listed in Table S7, and the kanamycin resistance gene *aph* was amplified by PCR from the pUCK1 plasmid using primers listed in Table S7 (Menard et al., 1993). The 3 PCR products and pFLP2 vector were assembled together using Gibson assembly (New England Biolabs) and sequence verified (Hoang et al., 1998). pFLP2 was then electroporated into *A. baumannii*, plated onto LB Km 40 agar, and grown overnight at 37°C. Transformants were patched to LB Km40 or LB agar with 10 % sucrose to isolate Km^R and $sucrose^S$ merodiploids. Merodiploid strains were grown in LB supplemented with 10 μg/mL riboflavin overnight at 37°C to resolve the plasmid. Cultures were serially diluted, plated on LB agar with 10 % sucrose, and incubated at 37°C overnight. The resulting Km^R $sucrose^R$ strains were screened for loss of *ribBX* and replacement with *aph* by multiple PCR reactions.

A. baumannii Expression Construct Generation

The *ribBX* gene was amplified from WT *A. baumannii* genomic DNA using primers listed in Table S7 and incorporated a C-terminal cMyc tag. The amplified gene product was ligated into digested pWH1266 containing the constitutive *r01* promoter, which was generated as previously described (Mortensen et al., 2014): the 16s gene *r01* was amplified from *A. baumannii* genomic DNA and ligated into the pWH1266 expression vector. The integrity of the *r01* promoter and *ribBX* was confirmed by sequencing. The empty vector and the *ribBX* expression vector were transformed into WT and *ΔzigA* by electroporation.

Growth in Calprotectin or Metal Chelators

Overnight *A. baumannii* cultures started from independent colonies as replicates were subcultured 1:50 in LB for 1 h. Back-diluted cultures were then inoculated 1:100 into LB containing various concentrations of tetrakis-(2-pyridylmethyl)ethylenediamine (TPEN) as indicated, and growth was monitored over time. For growth in medium containing recombinant human WT CP, back-diluted cultures were inoculated 1:100 into LB containing 40% CP buffer (20 mM Tris-HCl pH 7.5, 100 mM NaCl, 5 mM β-mercaptoethanol, 3 mM $CaCl_2$) supplemented with CP, and growth was monitored over time. To assess growth during Fe limitation, back-diluted cultures were inoculated 1:100 into M9 minimal media supplemented with 0.5% sodium succinate dibasic hexahydrate and 10 μM ethylenediamine-di(*o*-hydroxyphenylacetic acid) (EDDHA, LGC Standards), and growth was monitored over time.

ICP-MS Quantification of Total Metals

The quantification of total metal content of the growth media used here (LB + 40 % CP buffer) and total cell-associated metal was carried out largely as described before on a Perkin-Elmer Elan DRCII ICP-MS (Nairn et al., 2016). Briefly, the growth media was incubated with 200 μg/mL calprotectin (CP) at 37°C for 2 h. CP was then removed via filtration with a pre-washed and pre-equilibrated 3 or 10 kDa filter with the flow-through eluent analyzed for total metal content and compared with the same media prior to filtration, essentially as described (Nakashige et al., 2015). The CP used for these studies contained 0.11 protomer mol•equiv Zn, 0.08 protomer mol•equiv Cu, 0.01 protomer mol•equiv Mn, 0.03 protomer mol•equiv Ni and 0.04 protomer mol•equiv Fe and is thus 85% metal-free (2 metal sites per protomer); quantitation of the total metal chelated by CP in replicate experiments was found to be 95 ±7% of expected value based on the concentration of CP-binding sites (site 1 + site 2, per protomer). For bacterial lysates, strains were grown in the presence of the 200 μg/mL CP as described above. Cells were normalized to the same OD_{600} and pelleted at 4°C, then washed 3 times with ice-cold, chelexed PBS buffer. Cell pellets were stored at –80°C before measurements. Samples were incubated with 30% nitric acid at 95° for 10 min and 65°C for 1 h. The volumes were then adjusted to 3 mL with 2.5% nitric acid and subjected to elemental quantification on a Perkin-Elmer Elan DRCII ICP-MS equipped with AS-93 autosampler run alongside elemental standards. Cellular metal content was normalized to protein amount which was measured using a standard Bradford assay, as described previously (Jacobsen et al., 2011).

RNA Sequencing

WT *A. baumannii* was grown overnight in 3 mL LB. Cultures were reseeded 1:50 in LB and grown for 1 h at 37°C with shaking. These cultures were reseeded 1:100 in 40 % LB, 60 % CP buffer plus or minus 250 μg/ml CP and grown for 7 h at 37°C with shaking. Cultures were pelleted at 4°C with 2,500 x *g* for 8 min and then air dried on ice. Each pellet was suspended in 1 mL TRIzol and transferred to tubes containing lysing matrix B (MP Biomedicals). Bacteria were lysed using a FastPrep-24 (MP Biomedicals) bead beater for 45 s at 6 m/s. Two hundred μL chloroform then was added to each tube. After brief vortexing, the tubes were centrifuged for 15 min at 4°C and the upper layer was transferred to another new tube. RNA was purified using the RNeasy preparation kit (Qiagen) according to the RNeasy lipid tissue directions. DNA contamination was removed by adding 8 μL RQ1 (Promega), 12 μL 10x RQ1 buffer, and 2 μL RNase inhibitor (Promega) to each sample and incubating at 37°C for 2 h. Samples were then cleaned up using the RNeasy miniprep RNA cleanup protocol (Qiagen). To ensure purity of the RNA from DNA contamination, an aliquot of RNA was removed for reverse transcription (RT), including no-RT controls, and assessed by PCR. Prior to sequencing, RNA was quantified on the Synergy 2 with Gen5 2.00 software (BioTek).

Vanderbilt Technologies for Advanced Genomics Core Facility (VANTAGE) prepared RNA-seq libraries from 1.5 μg of *A. baumannii* total RNA using the following protocol. The integrity of the total RNA was evaluated using the Agilent Bioanalyzer Nano RNA chip. The Ribo-Zero rRNA removal kit for Gram-negative bacteria (Epicentre) was used to remove rRNA by following the manufacturer's protocol. The rRNA-reduced RNA was used as an input to the TruSeq stranded mRNA sample preparation kit (Illumina), skipping the mRNA selection step and going directly into the RNA fragmentation and random hexamer priming step. The RNA was converted into double-stranded cDNA, adapter ligated, and enriched with PCR, replacing the enzyme from the kit with KAPA HiFi DNA polymerase to create the final cDNA sequencing library. The cDNA library underwent quality control (QC) by running on an Agilent Bioanalyzer HS DNA assay to confirm the final library size and on an Agilent Mx3005P quantitative PCR (qPCR) machine using the KAPA Illumina library quantification kit to determine concentration. A 2 nM stock was created, and samples were pooled by molarity for multiplexing. From the pool, a 10.5 pM concentration was loaded into each well for the flow cell on the Illumina cBot for cluster generation. The flow cell was then loaded onto an Illumina HiSeq 2500, utilizing v3 chemistry and HTA 1.8 for a paired-end 50-bp run. The raw sequencing reads in BCL format were processed through CASAVA-1.8.2 for FASTQ conversion and demultiplexing. The RTA chastity filter was used, and only the PF (pass filter) reads were retained for further analysis.

Transcriptomic Analysis

The Illumina HiSeq 2500-generated FASTQ reads were processed by using the Bayesian adapter trimmer Scythe (version 0.992; http://github.com/vsbuffalo/scythe) to trim 3= adaptor sequence contaminants from the reads. EDGE-pro v1.3 (Estimated Degree of Gene Expression in Prokaryotes) software (Magoc et al., 2013) then was used to align the reads with Bowtie2 v2.1.0 (Langmead and Salzberg, 2012) and estimate gene expression directly from the alignment output. The FASTA of the reference genome sequence (.fna), protein translation table with coordinates of protein coding genes (.ptt), and a table containing coordinates of tRNA and rRNA genes were downloaded from NCBI (ftp://ftp.ncbi.nih.gov/GenBank/genomes/Bacteria/Acinetobacter_baumannii_ATCC_17978_uid17477). The .fna, .ptt, and .rnt files were concatenated from the main genome and two native plasmids into single input files, and they were used as inputs into EDGE-pro. EDGE-pro was run with default parameters, except for defining the read length as 50 bp (-l 50) and using 16 threads (-t 16) on a 64-core Linux server. On average, more than 96% of the reads were uniquely aligned. Alignment statistics and other QC metrics were calculated from the aligned BAM file using the RSeQC program suite (Wang et al., 2012). The output of EDGE-pro was an RPKM value table for the genome and plasmids. A script provided with EDGE-pro called edgeToDeseq.perl was used to concatenate the output of the various samples into a single count table for input into DESeq. The expression level of each gene was determined using DESeq (Anders and Huber, 2010) in the statistical programming package R-3.0.0 (http://www.r-project.org). Differences in expression comparing untreated WT *A. baumannii* to CP-treated *A. baumannii* were considered significant based on a *P* value less than or equal to 0.01.

Quantitative RT-PCR

Overnight cultures of *A. baumannii* were diluted 1:50 in LB and grown for 1 h at 37°C. Cultures were then diluted 1:100 into LB plus or minus 250 μg/ml CP and grown for 8 h. Cultures were pelleted at 4°C and resuspended in 1:1 acetone : ethanol prior to storage at -80°C until processing. For RNA extraction, cells were pelleted and resuspended in LETS buffer and lysed using Lysis Matrix B tubes (MP Biologicals) and a FastPrep-24 (MP) bead beater. Samples were heated to 55°C for 5 min and pelleted at 15,000 rpm for 10 min. The top phase was combined with TRIzol and incubated at room temperature for 5 min. Chloroform was mixed with each sample, incubated for 3 min, and centrifuged for 15 min at 4°C at 15,000 rpm. Following centrifugation, the upper aqueous phase was transferred to a new tube and incubated with isopropyl alcohol for 10 min at room temperature to precipitate the RNA. Samples were centrifuged at 4°C for 10 min at 15,000 rpm. Supernatant was removed, and the pellet was washed twice with 70% ethanol and dissolved in water. DNA contamination was removed by adding RQ1 and RQ1 buffer (Promega), and RNAse inhibitor (Thermo), and the samples were incubated at 37°C for 2 h. Following DNAse treatment, RNA was purified using RNease mini kit (Qiagen) following manufacturer's recommendation. RNA was quantified, and 2 μg of RNA was used for cDNA synthesis. cDNA synthesis and qRT-PCR was performed as previously described using the $2^{\Delta\Delta CT}$ method (Mortensen et al., 2014; Nairn et al., 2016). Primers used for qRT-PCR are listed in Table S7.

LC-MS/MS Proteomic Analysis

Protein samples were denatured in 8 M urea, 100 mM ammonium bicarbonate solution, then incubated for 45 min at 56°C with 10 mM dithiothreitol (DTT) to reduce cysteine residues. The free cysteine residue side chains were then alkylated with 40 mM iodoacetamide for 1 h in the dark at room temperature. The solution was diluted to 1 M urea and 1:100 (w:w) ratio of trypsin was added and the samples were digested at 37°C overnight. Peptides were desalted by Zip-tip and injected into an Easy-nLC HPLC system coupled to an Orbitrap Fusion Lumos mass spectrometer (Thermo Scientific, Bremen, Germany). Peptide samples were loaded onto a home-made C18 trap column (75 μm × 20 mm, 3 μm) in 0.1% formic acid. The peptides were separated using an Acclaim PepMapTM RSLC C18 analytical column (75 μm × 150 mm, 2 μm) using an acetonitrile-based gradient (Solvent A: 0% acetonitrile, 0.1% formic acid; Solvent B: 80% acetonitrile, 0.1% formic acid) at a flow rate of 400 nL/min. A 30 min gradient was implemented as follows: 0-0.5 min, 2-9% B; 0.5-24 min, 9-26% B; 24-26 min, 26-100% B; 26-30 min, 100% B followed by re-equilibration to 2% B. The electrospray ionization was carried out with a nanoESI source at a 260°C capillary temperature and 1.8 kV spray voltage. The mass spectrometer was operated in data-dependent acquisition mode with mass range 400 to 1600 m/z. The precursor ions were selected for tandem mass (MS/MS) analysis in Orbitrap with 3 sec cycle time using HCD at 35% collision energy. Intensity threshold was set at $5e^3$. The dynamic exclusion was set with a repeat count of 1 and exclusion duration of 30 s. The resulting data were searched against an *Acinetobacter baumannii* database (Uniprot UP000094982, 3,780 entries, with the database downloaded on 07/06/2017 from Uniprot) in Proteome Discoverer 2.1. Carbamidomethylation of cysteine residues was set as a fixed modification. Protein N-terminal acetylation, oxidation of methionine, protein N-terminal methionine loss, protein N-terminal methionine loss and acetylation, and pyroglutamine formation were set as variable modifications. A total of 3 variable modifications were allowed. Trypsin digestion specificity with two missed cleavage was allowed. The mass tolerance for precursor and fragment ions was set to 10 ppm and 0.6 Da respectively.

Statistical Rationale and Bioinformatics Analysis

Data analysis was performed as previously described (Kentache et al., 2017; Park et al., 2014). Proteins detected fewer than 3 times in 4 replicate lysates were excluded from our statistical analysis. The statistical analysis of these data was completed using unpaired, two-tailed student's *t* test with Welch's correction. Functional information for the selected proteins were gathered from the National Center for Biotechnology Information (NCBI, https://www.ncbi.nlm.nih.gov/) and the SEED database (http://pubseed.theseed.org/?

page=Minimal) (Overbeek et al., 2005). Metabolism pathway information for the selected proteins were obtained from the Kyoto Encyclopedia of Genes and Genomes (KEGG) database (https://www.genome.jp/kegg/pathway.html).

Siderophore Quantification

Siderophore production was quantified using a Chrome Azurol S (CAS) assay as described previously (Alexander and Zuberer, 1991; Schwyn and Neilands, 1987). Briefly, *A. baumannii* was grown for 36 h in the presence of 250 μg/mL CP or buffer as described above. Supernatants were collected and filtered through a 0.22 μm filter (Millipore). Supernatants were mixed 1:1 with the chrome azurol S shuttle solution(Alexander and Zuberer, 1991), and OD_{630} was determined after a 30 min incubation at room temperature. Values were normalized to starting cell density as determined by OD_{600}.

Zinc Proteome Prediction of *A. baumannii*

Using a previously published approach (Valasatava et al., 2016), we created two libraries of Hidden Markov Model profiles (Eddy, 1998): a library of Zn-binding Pfam domains (Finn et al., 2014), and a library of Zn-binding structural motifs. The Pfam domain library was created by merging two lists: 1). a list of Pfam domains with known 3-dimensional structure that contain a Zn-binding site extracted from MetalPDB (Putignano et al., 2018) in which each of these domains could be associated with the residues responsible for Zn-binding and with their positions within the domain sequence and 2). a list of Pfam domains without a known 3D structure but annotated as Zn-binding, obtained by text mining of the annotations in the Pfam database. The procedure resulted in a set of 573 Pfam domains: 541 with an associated Zn-containing 3D structure, and an additional 32 annotated as Zn-binding domains. The library of Zn-binding structural motifs was created by splitting into fragments the Zn-binding sites stored in MetalPDB as of June 2017, as previously described (Rosato et al., 2016). Only one representative was kept for Zn-binding sites that, though found in different PDB structures, fall in the same position of the same protein domain. Sites that are not physiologically relevant based on literature inspection, e.g., Zn-substituted structures, spurious sites, were manually removed from the dataset. This procedure resulted in a set of 6450 zinc-binding motifs derived from 2651 Zn-binding sites.

The Zn proteome of *Acinetobacter baumannii* was obtained by using the hmmscan tool (Eddy, 1998) to search each bacterial sequence for the profiles contained in the two libraries. A bacterial sequence was identified as containing a potential Zn-binding site if at least one of the following conditions was verified: A) The profiles of all the fragments of a given site matched the sequence with an e-value lower than 10^{-3} and the corresponding ligands are conserved in the sequence. B) The profile of a domain with associated ligands matched the sequence with an e-value lower than 10^{-5} and the ligands are conserved in the sequence. C) The profile of a domain with no associated ligands matched the sequence with an e-value lower than 10^{-7}. These predictions were integrated by adding the proteins annotated as Zn-binding in the UniProt database (UniProt Consortium, 2018). In total, 213 proteins of *Acinetobacter baumannii* were identified as Zn-binding proteins.

FAD Quantification

Overnight *A. baumannii* cultures were back-diluted 1:50 into LB for 1 h. Cultures were then inoculated 1:100 into LB containing 40% CP buffer (20 mM Tris-HCl pH 7.5, 100 mM NaCl, 5 mM β-mercaptoethanol, 3 mM $CaCl_2$) supplemented with 200 μg/ml CP and grown for 6 h. Optical densities were normalized across strains, and cells were pelleted and washed with PBS. Total cellular FAD was quantified using the FAD assay kit (Abcam). Pellets were resuspended in FAD assay buffer and lysed twice using Lysis Matrix B tubes (MP Biologicals) and a FastPrep-24 (MP) bead beater. Supernatants were collected, and protein concentration was determined by BCA assay (Thermo Scientific). Samples were deproteinized by adding ice-cold 4 M perchloric acid and incubated on ice for 5 min. Samples were centrifuged for 2 min at 4°C at 13,000 x g, and supernatants were transferred to a new Eppendorf tube. Ice-cold 2 M potassium hydroxide was added until the pH was 6.5-8. Samples were centrifuged for 15 min at 4°C at 13,000 x g, and supernatants were collected. To quantify FAD, 50 μL reaction mixtures were prepared by combining 46 μL of 1:50 dilution of sample with 2 μL OxiRad probe and 2 μL enzyme mixture (Abcam). OD_{570} was monitored over 30 min, and values were plotted against an FAD standard curve and normalized to total protein. Data are averaged from 3 independent experiments.

Purification of *A. baumannii* Proteins

Oligonucleotide primers used for cloning are listed in Table S7. The gene sequences of *ribA, ribB* and *ribBX* from *Acinetobacter baumannii ATCC 17978* (locus tags A1S_3107, A1S_0823 and A1S_3388, respectively) were obtained from the SEED database. The gene *ribBX* encodes a 373 amino acid protein that is 41% identical and 56% similar to the homolog encoded by *Mycobacterium tuberculosis* H37Rv (locus tag Rv1415; NP_215931; PDB: 4I14) over their entire length (Figure S4B) (Singh et al., 2013). The calculated molecular mass and theoretical isoelectric point (pI) value for the *A. baumannii* RibBX are 40,899 Da and 5.62, respectively (https://web.expasy.org/protparam/). Full length proteins were cloned into a pHIS plasmid at the *Nco*I site using an isothermal assembly method and was expressed with an N-terminal His-tag (Gibson et al., 2009).

These resulting plasmids were transformed into *E. coli* BL21(DE3) for expression. Cells were grown in Luria–Bertani (LB) medium supplemented with 100 μg/mL ampicillin and shaking at 37°C to OD_{600} of 0.6, at which time ITPG was added to final 0.5 mM. The cells were allowed to induce at 16°C overnight. For each 0.8 L cell pellet, cells were suspended in 40 mL lysis buffer (25 mM Tris, 500 mM NaCl, 2 mM TCEP, pH 8) and sonicated at 60 % power (3 s on; 9 s off, on ice), for total 15 min/L cells. This solution was centrifuged at 10,000 g (20 min, 4°C). The supernatant was filtered with 0.22 μm for loading onto a 5 mL HisTrap column (GE

Healthcare). The Ni-NTA column was run at 3 mL/min, and protein was eluted with a 4-40% buffer B (25 mM Tris, 500 mM NaCl, 2 mM TCEP, pH 8) gradient over 20 column volumes. The protein-containing fractions were pooled, cleaved with TEV protease and dialyzed again buffer (25 mM Tris, 500 mM NaCl, 2 mM TCEP, pH 8) at 4°C overnight. Solutions were filtered with 0.22 μm and run through Ni-NTA column. Non-tagged protein factions are pooled and concentrated to ~3 mL for loading on Hi Load™ 16/600 Superdex™ 200 or 75 (GE Healthcare). Running buffer was (25 mM Tris, 200 mM NaCl, 2 mM TCEP, pH 8), and protein was eluted at a flow-rate of 1 mL/min. Protein-containing fractions were pooled, concentrated and flash-frozen in liquid nitrogen, stored at –80°C, and buffer exchanged prior to use. Protein mass was confirmed by LC-ESI-MS or trypsin digested MALDI-MS and was judged to be 90% pure by overloaded SDS-PAGE gels. For RibBX, the residual FMN bound to RibBX during purification was confirmed by LC-MS/MS and UV-Vis spectroscopy.

GCHII Activity Assay

The GTP cyclohydrolase II (GCHII) activities of RibA and RibBX were measured essentially as previously described (Singh et al., 2013). Briefly, reaction mixtures were prepared in a buffer containing 50 mM Tris, 100 mM NaCl, 10 mM $MgCl_2$, 2 mM TCEP, 10 μM $ZnSO_4$, pH 8.0 in a total volume of 200 μL, with reactions initiated by the addition of enzyme to a final concentration of 2 μM with 0~1 mM GTP. To monitor the formation of 2,5-diamino-6-ribosylamino-4(3*H*)-pyrimidinone 5'-phosphate (DARP), the absorbance at 310 nm was monitored at 37°C for 20 min and the concentration of DARP was calculated using an extinction coefficient of Abs_{310} = 7.43 $mM^{-1}cm^{-1}$. The linear range of these kinetic traces was used to calculate the initial rate and these rates were used to fit to the Michaelis-Menten steady-state model.

DHBPS Activity Assay

The 3,4-dihydroxy-2-butanone 4-phosphate synthase (DHBPS) activities of RibB and RibBX were measured by a colorimetric method as described (Singh et al., 2013). Briefly, reaction mixtures contained 50 mM Tris, 150 mM NaCl, 10 mM $MgCl_2$, pH 7.5 in a total volume of 60 μL. Reactions were initiated by the addition of enzyme to final 1 μM with final 0~1 mM ribulose-5-phosphate (Cayman). After incubation at 37°C for 15 min, 48 μL of a saturated creatine (Fisher Scientific) solution was added, followed immediately by 24 μL 1-naphthol (Fisher Scientific) (dissolved at 35 mg/mL in 1 M NaOH). The absorbance at 525 nm was measured after 45 min using plate reader (BioTek, Synergy Neo2). The standard curve was constructed with 0~500 μM 2,3-butadione (Sigma-Aldrich) for calculating product (DHBP) formation. Initial rates were calculated for Michaelis-Menten fit. Inhibition of FMN was measured in the presence of 0~1 mM FMN (Cayman).

FMN Binding by ITC

All ITC titrations were carried out as described before (Grossoehme and Giedroc, 2009) using a MicroCal VP-ITC calorimeter. 300 μM FMN was placed into the syringe with ~30 μM RibBX protomer in the reaction cell. Injections (2~8 μL) were made at a rate of 2 $\mu L\ s^{-1}$, with 180~240 s allowed for equilibration of the mixture between injections. All reactions were conducted in at least triplicate in 50 mM Tris, 150 mM NaCl, 10 mM $MgCl_2$, pH 7.5 at 25.0°C. The Origin 7.0 Software package provided by MicroCal was used and data were fitted as single-site binding model with the n and K_a values optimized during the fit.

Crystal Structure of RibBX

RibBX expressed and purified as described above was subjected to polishing on a Superdex 200 10/300 GL column (GE Healthcare) running in 25 mM Tris, 200 mM NaCl, 2 mM TCEP, pH 8.0 at a flow-rate of 0.5 mL/min. Peak fractions were concentrated to 8~12 mg/mL using an Amicon centrifugal concentrator with a 30 kDa cutoff membrane (Millipore) and used for crystallization by vapor-diffusion in 96-well sitting-drop plates. Initial crystallization screening was carried out using commercial kits from MemGold2™ (Molecular Dimensions) by mixing 0.15 μL reservoir buffer and 0.15 μL protein solution and equilibrating against 30 μL reservoir buffer at 293 K. Small crystals appeared after 1 day when RibBX was equilibrated against a reservoir solution containing 10 mM MES, 100 mM NaCl, 150 mM ammonia sulfate, 19% (w/v) PEG 1000. The crystallization conditions were optimized over 19~24% (w/v) PEG1000 over 10~15 mg/mL RibBX while changing the protein:buffer ratio to 2:1 by hanging drop vapor diffusion. The plates were incubated at 20°C for 1-2 weeks, with crystals appearing before that time.

Crystals were harvested after 4-7 days, cryo-protected in the reservoir solution supplemented with 25% glycerol and flash frozen in liquid nitrogen. Diffraction data were collected at 100 K at the Beamline station 4.2.2 at the Advanced Light Source (Berkeley National Laboratory, CA) and were indexed, integrated, and scaled using XDS (Kabsch, 2010). The structure was solved by molecular replacement using PHASER the PDB: 4I14 as search model. The Autobuild function was used to generate a model that was improved by iterative cycles of manual building in Coot (Emsley et al., 2010) and refinement using PHENIX (Adams et al., 2010). Torsion-angle non-crystallographic symmetry restraints and secondary structure restraints were used during refinement. MolProbity software (Chen et al., 2010) was used to assess the geometric quality of the models. PyMOL (PyMOL Molecular Graphics System, Version 1.2r3pre, Schrödinger, LLC.) was used to generate molecular images. Data collection and refinement statistics are indicated in Table S6.

Analytical Gel Filtration Chromatography

A Superdex 200 10/300 GL column (GE Healthcare) was equilibrated and chromatographed in 50 mM Tris, 150 mM NaCl, 10 mM $MgCl_2$, 2 mM TCEP, pH 7.5 at a flow-rate of 0.5 mL/min and calibrated with the Gel Filtration Calibration Kit HMW

(GE Healthcare). A linear fit a plot of K_{av} vs. log M_r gave R^2 = 0.90. 100 μM RibBX was pre-incubated with 1.25 eq. FMN at 4°C for 1 h. 100 μL samples were injected for each chromatography run.

A. baumannii Growth with Riboflavin

Overnight cultures of *A. baumannii* were subcultured 1:50 in LB for 1 h. Cultures were then inoculated 1:100 into M9 minimal media supplemented with Vishniac's trace metal mix with or without $ZnCl_2$ as previously described (Nairn et al., 2016). M9 minimal media supplemented with full Vishniac's trace metal mix contained 36 μM Fe, 5.2 μM Mn, 3.2 μM Cu, 1.8 μM Mo, 13.4 μM Co and 27.2 μM Zn. Sodium succinate dibasic hexahydrate (Sigma) or sodium fumarate dibasic (Sigma) were used as the sole carbon source at 0.5 % (w/v). Riboflavin (Sigma) was supplemented with a final concentration of 10 μg/mL, and OD_{600} was monitored over time. Data are representative of at least 3 independent experiments.

QUANTIFICATION AND STATISTICAL ANALYSIS

Bioassays were performed with at least 3 biological replicates (n=3) as indicated. The averages and standard deviation of the separate replicates and Student's t test were then calculated using Graphpad Prism and Microsoft Excel. The structure of RibBX was refined with internal statistical analysis as reported in the deposition in the PDB. Detailed quantification and statistical analysis are fully described in the manuscript Figure legend and STAR Methods sections of the manuscript.

DATA AND SOFTWARE AVAILABILITY

The coordinates for the RibBX crystal structure have been deposited in the Protein Data Bank PDB: 6MNZ. Software used to analyze RNA sequencing results are fully described in the manuscript STAR Methods section with appropriate citations, and data have been uploaded to the National Institutes of Health Gene Expression Omnibus with accession number GSE125491 (https://www.ncbi.nlm.nih.gov/geo/query/acc.cgi?acc=GSE125491). Briefly, raw sequencing reads were processed using CASAVA-1.8.2 for FASTQ conversion. FASTQ reads were processed using the Bayesian adapter trimmer Scythe version 0.992. EDGE-pro version 1.3 was used to align reads with Bowtie2 version 2.1.0. The expression level of each gene was determined using DESeq in the statistical programming package R-3.0.0. Software used for diffraction data are fully described in the manuscript STAR Methods section with appropriate citations. Briefly, diffraction data were collected at 100 K at the Beamline station 4.2.2 at the Advanced Light Source (Berkeley National Laboratory, CA) and were indexed, integrated, and scaled using XDS (Kabsch, 2010). Software used for LC-MS/MS data is xcaliber v4.0. All software used in this study are reported in Methods Details and indicated in the Key Resources Table.